Combined PARP14 Inhibition and PD-1 Blockade Promotes Cytotoxic T Cell Quiescence and Modulates Macrophage Polarization in Relapsed Melanoma

Rotem Leshem[1,2,$], Kieran N. Sefton[1,2,$], Chun Wai Wong[1,2,3,4], I-Hsuan Lin[5], Dervla T. Isaac[6], Mario Niepel[6], and Adam F.L. Hurlstone[1,2,#]

[1]School of Biological Sciences, Faculty of Biology, Medicine and Health, The University of Manchester, Manchester, M13 9PT, UK

[2]Lydia Becker Institute of Immunology, The University of Manchester, Manchester, M13 9PT, UK

[3]Now at Massachusetts General Hospital Cancer Center, Department of Medicine, Massachusetts General Hospital, Harvard Medical School, Boston, MA, USA

[4]Now at Broad Institute of MIT and Harvard, Cambridge, MA, USA

[5]Bioinformatics Core Facility, The University of Manchester, Manchester, M13 9PT, UK

[6]Ribon Therapeutics Inc., 35 Cambridge Park Drive, Suite 300, Cambridge, MA 02140, USA

[$]These authors contributed equally

[#]To whom correspondence should be addressed: Dr Adam Hurlstone, Michael Smith Building, The University of Manchester, Dover Street, Manchester M13 9PT, UK; tel: +44 161 2751574; email: adam.hurlstone@manchester.ac.uk

Abstract

Programmed Cell Death 1 (PD-1) signaling blockade effectively restores immune surveillance to treat melanoma. However, chronic interferon-gamma (IFNγ) -driven immune homeostatic mechanisms in melanoma cells contribute to immune evasion and acquired resistance. We previously demonstrated that poly ADP ribosyl polymerase 14 (PARP14), an IFNγ-responsive gene product, in part mediates IFNγ-driven resistance, as its inhibition prolonged PD-1 blockade responses in preclinical models. Nevertheless, PARP14 inhibition alone could not achieve full tumor clearance, indicating additional resistance mechanisms. Herein, we identify a robust PARP14 catalytic inhibitor (PARP14i) gene signature associated with improved patient survival. We elucidate immune and tumor cell adaptations to PARP14 inhibition combined with PD-1 blockade using preclinical models. This combination therapy suppressed tumor-associated macrophages while increasing pro-inflammatory memory macrophages. Notably, it preserved cytotoxic T cell function by inducing a quiescent state, mitigating terminal exhaustion. Despite enhancing immune responses, adaptive resistance mechanisms emerged in tumor cells, engaging alternative immune evasion pathways. These findings indicate that this combination therapy primes immune cells for further therapeutic intervention, providing a promising strategy to overcome resistance and optimize treatment outcomes.

Keywords: PARP14, T cell exhaustion, quiescent T cells, memory macrophages, adaptive resistance

Summary

While immune checkpoint inhibitors, such as α-PD-1 therapy, provide significant clinical benefits, many tumors develop resistance and relapse. Re-treatment with α-PD-1 often fails because T cells lose their function (a process called exhaustion), and immune-suppressing cells like tumor-associated macrophages (TAMs) increase in the tumor environment, enabling tumors to evade immune attack.

Recent studies have shown that a small molecule inhibitor of PARP14 can restore sensitivity to α-PD-1 therapy by remodeling the tumor environment. This includes increasing immune cell infiltration and improving antigen presentation, which helps the immune system recognize tumor cells.

Using single-cell RNA sequencing, we discovered that this therapy induces a new state of T cell dormancy, where cytotoxic T cells temporarily stop attacking but retain the potential to be reactivated by additional treatments. This finding opens new opportunities to sustain immune responses and improve outcomes for patients who relapse after immunotherapy.

62 **Introduction**

63 Drugs antagonizing the PD-1 signaling axis by disrupting the interaction between PD-1 on
64 exhausted T cells and Programmed Cell Death Ligand 1 (PD-L1) on tumor and stromal cells
65 have vastly improved outcomes for high-risk and late-stage melanoma patients. However,
66 among responders to PD-1 blockade therapy, approximately 25% will relapse within two
67 years of initiating treatment [1]. Little can be done at present for these patients. Analysis of
68 relapsing tumors has revealed that 30% are characterized by intrinsic—that is, ligand-
69 independent— interferon-gamma (IFNγ) signaling [2]. Intrinsic IFNγ signaling in cancer cells
70 has been shown to follow chronic IFNγ stimulation and to entail epigenetic remodeling
71 wherein signal transducer and activator of transcription 1 (STAT1) and Interferon Regulatory
72 Factor 3 (IRF3) permanently occupy the regulatory sites of a subset of interferon-stimulated
73 genes (ISG), including notably those promoting T cell dysfunction [3]. Indeed, the ISG
74 selectively upregulated in chronically stimulated cancer cells (ISG resistance signature or
75 ISG.RS) predicts poor survival in patients and poor response to PD-1 blockade [4].

76

77 Our previous work revealed a contribution from PARP14 in mediating chronic IFNγ
78 stimulation-driven PD-1 blockade resistance in preclinical models [5]. One model we
79 developed entailed implantation of the mouse rapidly accelerated fibrosarcoma homolog B
80 (BRAF) and Phosphatase and Tensin homolog (PTEN) mutant melanoma cell line YUMM2.1
81 [6] into the hypodermis of syngeneic C57/BL6 mice, and then treating these mice with a
82 short course of anti-PD-1 (α-PD-1) antibodies when tumors became palpable. In tumors that
83 resumed growth following α-PD-1 treatment, we observed increased expression of multiple
84 ISG, including ISG.RS genes, relative to control (untreated) tumors and to tumors still
85 responding to PD-1 blockade therapy [5]. AI-assisted immune profiling, based on

86 deconvolving gene expression, indicated that relapsing tumors were also relatively more T
87 cell infiltrated, including by T_{EM} and $T_{CM.}$ However, these T cells were also more dysfunctional
88 [5]. The regrowth of such tumors was significantly delayed—but not abolished— and
89 survival lengthened by adding a highly potent and selective PARP14 inhibitor RBN012759
90 (PARP14i, Ribon Therapeutics)[7] to the treatment regimen [5].
91
92 This previous study also highlighted that the *PARP14* gene is a STAT1 target and that PARP14
93 itself is a STAT1 interacting protein [5]. Moreover, in macrophages, PARP14 interaction with
94 STAT1 inhibits the expression of proinflammatory genes [8] but regulates IRF3 recruitment of
95 RNA polII to promoters of IRF3 target genes [9] and is thus positioned to influence the
96 expression of ISG. However, the details are far from clear. Certainly, our previous analysis of
97 gene expression indicated that PARP14 inhibitor treatment of melanoma cells chronically
98 stimulated with IFNγ increased IFN-, TNF-α-, and IL-6-driven inflammatory signaling [5].
99
100 Intrigued by the potential of PARP14 to influence the expression of ISG in tumor cells but
101 also the failure of PARP14 inhibitor treatment to permanently flatten tumor rebound after α-
102 PD-1 treatment, we undertook a detailed analysis of tumor composition and gene
103 expression changes attending PARP14 inhibitor treatment to identify other targets for
104 intervention which we now present below.
105
106

107 **Materials and Methods**

108 **Reagents**

109 Recombinant human IFNγ (PHC4031, Gibco) and recombinant mouse IFNγ (PMC4031,
110 Gibco). PARP14 inhibitor RBN012759 [7] and PARP14 PROTAC RBN012811 (Ribon
111 Therapeutics) [10].

112 **Cell lines**

113 Human melanoma cell lines A375 and 501-Mel (provided by Claudia Wellbrock, The
114 University of Manchester), MC38 cells (provided by Santiago Zelenay, The University of
115 Manchester) and YUMM2.1 cells (provided by Richard Marais, The University of Manchester)
116 were maintained in RPMI-1640 (Sigma–Aldrich) supplemented with 10% v/v fetal bovine
117 serum (Life Technologies) and 1% w/v penicillin-streptomycin (Sigma–Aldrich), at 37 °C in a
118 5% v/v CO_2 humidified incubator. Cell lines authenticated by STR profiling; cultures routinely
119 tested for mycoplasma. Cells were treated for two weeks with 50 IU/mL IFNγ, refreshed
120 every 2-3 days, and subsequently treated with 500nM DMSO (Sigma–Aldrich); 500nM
121 PARP14i; or 100nM PARP14 PROTAC for 48h.

122 **Mouse tumor implants**

123 Mice were housed in the Biological Services Facility of The University of Manchester on a
124 12/12 h light/dark cycle and given ad libitum food (Bekay, B&K Universal, Hull, UK) and
125 water. All procedures were approved by the University of Manchester's animal welfare
126 ethical review board and performed under relevant Home Office licenses according to the
127 UK Animals (Scientific Procedures) Act, 1986.

128 8–12-week-old C57BL/6 female mice (ENVIGO) were allowed 1-week to acclimatize.
129 YUMM2.1 cells (5×10^6 cells) in 100 µL serum-free RPMI-1640 were subcutaneously injected
130 into the left flank. Tumor volumes (height x width x length caliper measurements) and

131 mouse weights were monitored every 2–3 days. When tumors reached a volume of 80 mm^3,
132 mice were administered two doses of 300 µg α-PD-1 antibody (BioXCell) in 100 µL
133 InVivoPure pH 7.0 Dilution Buffer (BioXCell) via intraperitoneal (i.p.) injection administered
134 at 3-day intervals. Mice were culled if tumors remained under 100 mm^3 (total responders) or
135 conversely reached 800 mm3 (non-responders). Otherwise, mice with tumors recovering to
136 140 mm^3 were randomized to a second round of treatments (re-treatment): 2 doses of 300
137 µg of rat isotype control antibody IgG2b (BioXCell) (IgG group) or α-PD-1 antibody (BioXCell)
138 (α-PD-1 group) in 100 µL InVivoPure pH 7.0 Dilution Buffer (BioXCell) via i.p. injection at
139 three-day intervals, 14 doses of 500 mg/Kg of PARP14I by oral gavage twice a day (PARP14i
140 group), or a combination of α-PD-1 i.p. and PARP14i gavage in the same doses (Combination
141 group). PARP14i was dissolved in 0.5% w/v methylcellulose (Sigma–Aldrich) + 0.2% v/v
142 Tween 80 (Sigma–Aldrich). Dose volume - 10 mL/kg.

143 **Tumor immune infiltrate analysis by flow cytometry**

144 Tumors were dissected upon reaching 250-400mm^3 following retreatment and incubated
145 for 45 minutes with 100 µg/mL Liberase (Sigma–Aldrich) in serum-free media at 37 °C, then
146 pushed through a 100 µM nylon cell strainer. The cell suspension was stained for 20 min
147 with Zombie UV™ Fixable Viability Kit (BioLegend) in PBS. Subsequently, Fc receptors were
148 blocked, and cells were stained with a surface stain antibody mix. Cells were fixed and
149 permeabilized using the Foxp3/Transcription Factor Staining Buffer Set (eBioscience)
150 following manufacturer instructions. Samples were measured on a BD Fortessa flow
151 cytometer (BDBiosciences), and data was collected using BD FACSDiva™ software. For all
152 antibodies, a non-stained cell sample and appropriate fluorescence minus one control were
153 analyzed as well. Data were analyzed using FlowJo version 8.7.

154 Antibodies: CD16/32 (clone 93), CD45 (Cat. 103132), CD3ε (Cat. 100306), CD4 (Cat. 100552),
155 CD8α (Cat. 100742), PD-1 (Cat. 135231), LAG-3 (Cat. 125224), TIM-3 (Cat. 119721), Ki-67
156 (Cat. 652420), Granzyme B (Cat. 372214), CD69 (Cat. 104531), and CTLA-4 (Cat. 106338)
157 from Biolegend. Tox (Cat. 12-6502-82) was purchased from eBioscience. Gating strategy as
158 described in SUPPLEMENTARY FIGURE 5.

159 **Single-cell RNAseq sequencing**

160 **Tumor processing**

161 Tumors were collected on day 7 of retreatment into serum-free RPMI on ice, then minced
162 into 1mm pieces and incubated at 37 °C up to 60 min in Liberase TL (Millipore Sigma) with
163 rocking according to manufacturer instructions. Digestion was stopped using fetal bovine
164 serum, and tissue was further dissociated using a wide-bore pipette and filtered through a
165 cell strainer to achieve a single-cell solution. Immune population enrichment was done by
166 CD45 mouse Microbeads (Miltenyi) according to manufacturer instructions. Following
167 sorting, both populations were counted, and ~5% of CD45 negative cells were spiked back
168 into the CD45 positive fraction. Cells were fixed for 18 hours, then quenched and stored at -
169 80°C in Enhancer according to 10x Genomics Tissue Fixation & Dissociation for Chromium
170 Fixed RNA Profiling protocol (CG000553 Rev A) until all samples were collected.

171 **Single-cell isolation and library construction**

172 Gene expression libraries were prepared from formaldehyde-fixed samples using the
173 Chromium X and Chromium Fixed RNA kit, Mouse Transcriptome, 4 rxns x 16 BC (10x
174 Genomics, Inc.) according to the manufacturer's protocol (CG000527 Rev C). Illumina-
175 compatible sequencing libraries were constructed by adding P5, P7, i5, and i7 sample
176 indexes and Illumina Small Read 2 sequences to the 10x barcoded, ligated probe products
177 via Sample Index PCR followed by a SPRIselect size-selection.

178 **Sequencing**

179 The resulting sequencing library comprised standard Illumina paired-end constructs flanked
180 with P5 and P7 sequences. The 16 bp 10x Barcode and 12 bp UMI were encoded in Read 1,
181 while Read 2 sequenced the ligated probe insert, constant sequence, and the 8bp Probe
182 Barcode. Sample indexes were incorporated as the i5 and i7 index reads. Paired-end
183 sequencing (28:90) was performed on the Illumina NovaSeq6000 platform.

184 **Data Analysis**

185 **Raw data processing and cell filtering**

186 Raw sequencing data were processed using the 10x Genomics Cell Ranger pipeline (v7.0.0).
187 Base call (BCL) files generated by the sequencer were demultiplexed and converted to
188 FASTQ files using "cellranger mkfastq". The FASTQ files were then mapped against the pre-
189 built Mouse reference package from 10X Genomics (mm10-2020-A) using "cellranger multi"
190 to demultiplex and produce the gene-cell barcode matr-ix for individual samples. The single-
191 cell data were processed in R environment (v4.1) following the workflow documented in
192 Orchestrating Single-Cell Analysis with Bioconductor [11]. Briefly, for each sample, the HDF5
193 file generated by Cell Ranger was imported into R to create a SingleCellExperiment object. A
194 combination of median absolute deviation (MAD), as implemented by the "isOutlier"
195 function in the scuttle R package (v1.4.0), and exact thresholds were used to identify and
196 subsequently remove low-quality cells before data integration.

197 **Data integration, visualization, and cell clustering**

198 The log-normalized expression values of the combined data were re-computed using the
199 "multiBatchNorm" function from the bachelor R package (v1.10.0). The per-gene variance of
200 the log-expression profile was modeled using the "modelGeneVarByPoisson" function from
201 the scran R package (v1.22.1), and the top 5000 highly variable genes were selected. The

202 mutual nearest neighbors (MNN) approach implemented by the "fastMNN" function from
203 the bachelor R package was used to perform batch correction. The first 50 dimensions of the
204 MNN low-dimensional corrected coordinates for all cells were used as input to produce the
205 t-stochastic neighbor embedding (t-SNE) projection and uniform manifold approximation
206 and projection (UMAP) using the "runTSNE" and "runUMAP" functions from the scater R
207 package (v1.22.0) respectively. Putative cell clusters were identified using the Leiden
208 algorithm from the igraph R package (v1.3.0).

209 **Marker genes and differential expression analysis**

210 Cluster-specific markers were identified using the "findMarkers" function from the scran R
211 package, which performs pairwise t-tests between clusters. Differential expression analysis
212 between treatment and control (IgG) was performed on pseudo-bulk samples using the
213 quasi-likelihood pipeline from the edgeR R package (v3.36.0). Genes with a false discovery
214 rate (FDR) below 5% were considered differentially expressed.

215 **Pathway analysis**

216 Pathway enrichment analysis of differentially expressed genes was performed using the R
217 package enrichR (v3.0). Pathway results were ranked by the combined scores (calculated as
218 log(P-value) multiplied by z-score), and pathways with an adjusted P-value < 0.05 were
219 considered significant. Further gene set enrichment analysis GSEA was done using
220 Metascape web tool [12] and plotted as $-\log_{10}P$.

221 **Subclustering and further analysis**

222 Cells were divided into functional cell type groups and further subclustered using the
223 Louvain method for community detection [13]. Trajectory inference was made using the
224 Slingshot R package [14], and the association of our PARP14i signature with survival in
225 immune checkpoint blockade therapy(ICBT) cohorts, as well as a comparison of high and

226 low-expressed genes in specific clusters, was assessed using Tumor Immune Dysfunction
227 and Exclusion (TIDE) web tool [15]. Sample RL1i projection on UMAP was done using the
228 ProjecTILs R package [16].

229 **Data Availability**

230 Single-cell RNAseq data have been deposited in the ArrayExpress database at EMBL-EBI
231 under accession number E-MTAB-14471. Bulk RNA sequencing was performed as previously
232 described [5], with data available from the ArrayExpress database under accession numbers E-
233 MTAB-12195 and E-MTAB-12872.

234

235

236 **Results**

237 **A genetic signature reflecting the modulating effect of PARP14i on chronic IFNγ**
238 **stimulation predicts response to α-PD-1 in clinical cohorts**

239 We and others have previously implicated PARP14 in modulating type II interferon signaling
240 [5,8,17]. Following chronic stimulation of several mouse and human cancer cell lines with
241 IFNγ and then subsequent treatment for 48 hours with a PARP14 catalytic inhibitor
242 (PARP14i), PARP14 proteolysis targeting chimera (PROTAC), or aqueous Dimethyl sulfoxide
243 (DMSO; drug solvent control), we assessed differences in gene expression by bulk RNA
244 sequencing (RNAseq). Comparison of the top 50 differentially expressed genes within each
245 cell model revealed a shared expression pattern, which we narrowed down to a PARP14i
246 signature consisting of 30 genes **(FIGURE 1A, SUPPLEMENTARY FIGURE 1A and**
247 **SUPPLEMENTARY TABLE 1)**. Pathway enrichment analysis performed by Metascape [12] and
248 ARCHS4 [18] revealed that among this signature were genes strongly correlated with
249 response to IFNγ signaling, with an emphasis on STAT/IRF function **(FIGURE 1B and**
250 **SUPPLEMENTARY FIGURE 1B).** However, we found this signature is distinct from the genes
251 contained within the IFNγ signaling GO term, with less than half of the PARP14i signature
252 displaying overlap. We then investigated whether this PARP14i signature could predict
253 response to α-PD-1 therapy by employing Tumor Immune Dysfunction and Exclusion (TIDE)
254 analysis [15]. High expression of genes within this signature was associated with substantial
255 improvement in overall patient survival across several clinical cohorts receiving immune
256 checkpoint blockade therapy [19–21] **(FIGURE 1C)**, underscoring the prognostic value of this
257 signature and supporting the potential therapeutic benefit of PARP14 inhibition.

258

259 Furthermore, we performed RNAseq analysis on subcutaneous tumors comprising YUMM2.1
260 cells dissected from mice treated with either IgG or α-PD-1, dividing the latter into those
261 either relapsing or responding to the treatment. Although the PARP14i signature was
262 upregulated in α-PD-1-treated samples, it did not distinguish between treatment response
263 and relapse (**FIGURE 1D**). For further comparison, we also analyzed IgG-treated tumors
264 arising from YUMM2.1 cells pre-treated *ex vivo* with chronic IFNγ before implantation and
265 found that the PARP14i signature was significantly downregulated (**FIGURE 1D**), consistent
266 with a tumor microenvironment (TME) that is T cell cold and inherently resistant to α-PD-1
267 [5].
268

269 **Analysis of changes to the cellular composition of YUMM2.1 tumors relapsing following α-**
270 **PD-1 therapy driven by subsequent PARP14 inhibitor treatment**

271 To investigate further the ability of PARP14i to improve α-PD-1 response, we turned to our
272 previously described mouse model of acquired resistance [5]: YUMM2.1 cells were
273 implanted subcutaneously, and upon tumors reaching ~80mm^3 in volume, two doses of α-
274 PD-1 antibodies were given three days apart **(FIGURE 2A and SUPPLEMENTARY FIGURE 2A)**.
275 Tumor volumes were routinely recorded **(SUPPLEMENTARY TABLE 2),** and at ~100-150mm^3,
276 animals were randomly allocated into the following re-treatment groups: IgG2a (n=4); α-PD-
277 1 (n=3); PARP14i alone (n=3); and a combination of α-PD-1 + PARP14i (n=4). Animals were
278 sacrificed following seven days of re-treatment, and tumors were subsequently processed
279 for single-cell RNA sequencing (scRNAseq). Following tumor dissociation and enrichment for
280 CD45$^+$ cells, 5% from the CD45$^-$ cell fraction was added to ensure tumor cell representation

281 in our analyses. Cells were fixed and frozen until all tumor samples were collected; then,
282 samples were barcoded, multiplexed, and libraries prepared and sequenced.
283
284 In total, fourteen samples of tumor immune cells were sequenced. Initial analysis of
285 sequencing data identified one of the IgG samples (RL11i) to be anomalous, which upon
286 further review of its corresponding tumor growth curve was attributed to it being, in reality,
287 a non-responder to the initial α-PD-1 treatment, and therefore, it was excluded from
288 subsequent analyses (**SUPPLEMENTARY FIGURE 2A-C)**. Leiden unsupervised clustering
289 across the remaining thirteen treated samples identified twenty-eight clusters based upon
290 gene expression patterns, with a diverse range of cell types represented across samples and
291 treatment groups **(FIGURE 2B, SUPPLEMENTARY FIGURES 2C and D and SUPPLEMENTARY**
292 **TABLES 3-4)**. The following cell types were identified: Monocytes (Clusters 1-5);
293 Macrophages (6-8); B cells (9-10); Plasma cells (11); Natural Killer (NK) cells (12); T cells (13-
294 17); Dendritic cells (18-21); Granulocytes (22-25); Cancer-Associated Fibroblasts (26); and
295 Tumor cells (27-28). To characterize the individual clusters within these groups, we manually
296 validated cell type identity by comparing the expression of known markers across clusters
297 **(SUPPLEMENTARY TABLES 5-8)**.
298
299 Macrophages, Monocytes, and T cells were the most abundant leukocyte populations across
300 all treatment groups, with distinct subpopulations displaying treatment-specific enrichment
301 **(SUPPLEMENTARY FIGURE 2E)**. Notably, T cells were particularly abundant in combination-
302 treated samples, with increased prevalence of clusters 14 and 16 and depletion of cluster 13,
303 which was highly enriched in IgG-treated samples **(FIGURE 2C)**. Similarly, analysis by cell
304 density plots revealed a shift from cluster 7 in macrophages, prominent in α-PD-1-treated

305 samples, towards cluster 6 in the PARP14i and combination treatments **(FIGURE 2D)**.
306 Furthermore, we observed IgG-specific enrichment and depletion of B cells and monocytes,
307 respectively. Similarly, across our treatment cohort, few neutrophils and eosinophils were
308 identified, and these could not be well separated, yet we found the sequenced tumor
309 sample, which did not respond to α-PD-1 to be highly enriched in neutrophils
310 (**SUPPLEMENTARY FIGURE 2B**), consistent with a documented role of neutrophils in
311 promoting rapid tumor growth [22].
312

313 **PARP14 inhibitor treatment increases M1 macrophage polarization to generate a memory-**
314 **like state**

315 Given the previous demonstration that PARP14i can suppress the reprogramming of Tumor-
316 Associated Macrophages (TAMs) [23] that are widely considered to be pro-tumorigenic [24]
317 and mimics the effects of α-PD-1 treatment on macrophages in renal tumor explants [7], we
318 interrogated the effects of PARP14i upon the macrophage populations in the TME within our
319 specimens. By further subclustering clusters 1-8 from the initial analysis, we created a new
320 MonoMac UMAP representation detailing a clear division of these subclusters into those
321 that exhibited characteristics of classically activated (M1) macrophages (Left) or alternatively
322 activated (M2) macrophages (Right) (**FIGURE 3A** and **SUPPLEMENTARY TABLES 6, 11)**.
323

324 Analysis of cell type proportions within this subclustering revealed treatment-specific
325 changes. Combination treatment notably shifted macrophage polarization from M2 towards
326 M1 (**FIGURE 3B**). Further inspection of gene enrichment analysis of Differentially Expressed
327 Genes (DEGs), applied alongside cell density mapping, allowed us to robustly identify

328 subclusters most affected by treatment **(FIGURE 3C & D)**. This demonstrated that subcluster
329 10— the most abundant cluster in the IgG-treated samples— is effectively depleted by
330 Combination treatment. This subcluster consists primarily of TAMs, which are known to
331 facilitate tumor progression and metastasis, and as such, their reduction by Combination
332 treatment disrupts pro-tumoral mechanisms.
333
334 These anti-tumoral effects are further supported by the expansion of specific macrophage
335 subsets. We observed an increase in M1 macrophages (subcluster 2), signifying an enhanced
336 pro-inflammatory response that bolsters anti-tumor immunity. This increase highlights the
337 ability of Combination treatment to promote a macrophage phenotype that is associated
338 with effective immune surveillance and cytotoxic activity. Similarly, the increased abundance
339 of a transitory M1/M2 macrophage state (subcluster 4) further illustrates the dynamic
340 changes in macrophage populations, highlighting cellular plasticity modulated by
341 Combination treatment to influence the balance between inflammatory and
342 immunoregulatory activities. Concurrently, macrophages in subcluster 8, most closely
343 associated with an M2a macrophage identity, play a nuanced role in the TME under
344 combination treatment. These macrophages exhibit high expression of *Cxcl13* **(FIGURE 3E)**,
345 which can mediate both pro- and anti-tumoral effects. CXCL13 interaction with CXCR5 can
346 recruit cytotoxic T cells to the TME, promoting tumoricidal factor secretion and supporting
347 the formation of tertiary lymphoid structures [25,26]. Conversely, this axis can also enhance
348 IL-10 secretion by tumor cells, suppressing the pro-inflammatory functions of antigen-
349 presenting cells (APCs) or recruiting immunosuppressive cells [27]. In parallel, the expression
350 of *Ccl7* and *Cxcl1* by M2a may also contribute to pro-tumorigenic effects, such as promoting

351 angiogenesis and invasion [28,29], reflecting the dual functionality of this macrophage
352 subset in the TME.
353
354 The overall increase in M1 macrophages following Combination treatment is linked to
355 elevated expression of pro-inflammatory genes (e.g., *Tnf* and *Stat3*) **(FIGURE 3F)**, particularly
356 in subclusters 2 and 4, while the decreased expression of *Stat6* and *Jun* correlates with their
357 reduced transcriptional activity and cellular activation. These changes suggest subclusters 2
358 and 4 may represent memory-like cells with the potential for re-activation [30]. In contrast,
359 PARP14i treatment results in a marked downregulation of *Nfatc1*, *Nfatc3,* and *Smad4* across
360 subclusters, reducing *Tgfb1* signaling in M2 macrophage clusters, as evidenced by lower *Sox2*
361 and *Sox4* expression **(FIGURE 3F)** [31]. The depletion of key drivers of M2 macrophage
362 polarization such as *Tgm2*, *Vegfa,* and *Cebpb* [32] in clusters 8-11 by Combination treatment
363 aligns with an overall reduction in M2 macrophage populations. In the context of subcluster
364 8, however, which is enriched by Combination therapy, the reduced levels of anti-
365 inflammatory gene expression by these cells **(FIGURE 3F)** posits them as a transitional
366 macrophage state with reduced features of classical M2 macrophages, reinforcing a
367 Combination treatment-driven transition towards a more hostile tumor environment.
368
369 To further explore the molecular underpinnings of macrophage polarization, we applied
370 Single-Cell rEgulatory Network Inference and Clustering (SCENIC) analysis [33] to evaluate
371 transcriptional regulatory programs within these subclusters **(FIGURE 3G)**. Here, we
372 identified regulons that effectively delineated M1 (*Runx3* and *Cux1*) and M2 (*Irf4*)
373 macrophages. Additionally, six regulons associated with M2 macrophages (*Nfia, Nr1d1, Klf2,*
374 *Klf3, Etv1, Dbp*) were most strongly associated with subcluster 10. In the context of

375 Combination treatment, the depletion of subcluster 10 resulted in a significant reduction in
376 the activity of these regulons. However, this reduction may be offset by the enrichment of
377 subcluster 8, indicative of a directional shift in this treatment towards an M1-like phenotype.
378 These findings suggest that the overall balance between M1 and M2 macrophages is shifting
379 towards a pro-inflammatory, anti-tumor state in Combination treatment. Notably,
380 subclusters 2 and 4, despite their relatively low regulon activity beyond the M1-defining
381 features, may represent more memory-like macrophage states.
382

383 **PARP14 inhibitor treatment in combination with α-PD-1 therapy drives activated cytotoxic**
384 **T cells and limits their transition to dysfunctional states**

385 PARP14 (also known as ARTD8) has been shown to interact with STAT6, a transcription factor
386 activated by interleukin-4 (IL-4), to promote Th2 cell differentiation [34], while Hoon Cho
387 and colleagues demonstrated that PARP14 is involved in the regulation of antibody
388 responses, particularly IgA production, through promoting Th17 differentiation [35]. Both
389 Th2 and Th17 cells are implicated in immune dysfunction in tumors [36] Moreover, our
390 previous work demonstrated that chronic PARP14i treatment of stimulated T cells resulted in
391 increased percentages of IFNγ- and TNFα-producing CD4 and CD8 T cells, accompanied by
392 decreases in TGFβ and IL-10 [5], consistent with a shift toward a type 1 pro-inflammatory T
393 cell response in the TME.
394

395 To further characterize specific T cell identities and assess their functionality, we conducted
396 subclustering of clusters 12-17 from the initial clustering **(FIGURE 4A).** By combining NK and
397 T cells for further subclustering, we can be confident that our new T cell clusters are free

398 from any contaminating readouts due to the presence of NK T cells. This subclustering can
399 be split broadly into NK and NKT cells (1-5) and T cells (6-19), with key subpopulations
400 including naïve T cells (7 and 19), regulatory T cells (Tregs) (10 and 11), and cytotoxic T cells
401 (13-18). Comparing the proportions of each T cell subcluster revealed treatment-specific
402 changes in cellular identity and function **(FIGURE 4B and SUPPLEMENTARY TABLE 9).**
403
404 Cell density mapping **(FIGURE 4C)** highlighted a treatment-dependent decrease in naïve T
405 cells (subcluster 7), which were highly abundant in IgG-treated samples, suggesting their
406 transition into differentiated or activated states upon treatment. In accordance, in IgG-
407 treated tumors, naïve T cells (subcluster 7) exhibited high expression of *Ccr7* and *Ccr9*, which
408 likely mediated their recruitment to the TME **(FIGURE 4D)**. CCR7 facilitates migration toward
409 lymphoid tissues via CCL19, a chemokine produced by exhausted CD8+ T cells (subcluster
410 13) and M2a macrophages (MonoMac subcluster 8) [37]. This interaction may reflect a futile
411 attempt to restock the TME with tumor-inexperienced T cells. However, these naïve T cells
412 exhibited increased *Sell* expression compared to other T cell subclusters, indicative of early
413 activation **(SUPPLEMENTARY FIGURE 3A)** and that IgG-treated tumors suffer from
414 dysfunctional T cell priming by APCs.
415
416 Corroborating our hypothesis that the reduction in naïve T cells is due to their differentiation
417 into more active T cell states, we identified a significant enrichment of effector T cells
418 (subclusters 13–16) in the combination treatment group. These cells are recruited and
419 retained in the TME through interactions with pro-inflammatory chemokine ligands,
420 including CCL3, CCL4, and CCL5 **(FIGURE 4D)**[38]. This recruitment is further reinforced by
421 the CXCR5-CXCL13 axis, where CXCL13, predominantly produced by M2a macrophages in our

422 data as previously described (MonoMac subcluster 8), drives cytotoxic T cell recruitment to
423 the TME and aids the formation of tertiary lymphoid structures [25,26]. These structures
424 serve as immune activation hubs, enabling CXCR5-expressing effector T cells to undergo
425 further activation and proliferation, enhancing their cytotoxic function.
426
427 Subclusters 13–16 display distinct functional profiles associated with T cell exhaustion,
428 quiescence, hyperactivation, and T cell response, respectively (**FIGURE 4E &**
429 **SUPPLEMENTARY FIGURES 3B & C)**. In the context of anti-tumor activity, T cell subclusters
430 13-16 are closely interconnected in driving the T cell effector response. Our slingshot
431 trajectory analysis (**FIGURE 4F)** indicates that by entering a state of dormancy (subcluster
432 14), hyperactive T cells (subcluster 15) sidestep terminal exhaustion (subcluster 13) in the
433 presence of chronic antigen stimulation. Thereafter, quiescent cells can either undergo
434 reactivation (subcluster 16) or persist as a reservoir of memory T cells with retained effector
435 function, poised for re-activation.
436
437 TIDE analysis was performed using gene expression signatures arising from each T cell
438 subcluster from subclusters 13-16 **(SUPPLEMENTARY TABLE 10)**, revealing that high
439 expression of the gene signature for subcluster 16 (reactivated T cells) was associated with
440 significantly improved survival of patients receiving immune checkpoint blockade therapy
441 for either melanoma or bladder cancer (**FIGURE 4G and SUPPLEMENTARY FIGURE 3E)**.
442 Furthermore, we observed this was also true, albeit to a lesser degree, for the gene
443 signatures arising from subclusters 14 (quiescent T cells) and 15 (hyperactive T cells). On the
444 other hand, the gene signature of T cell subcluster 13 (exhausted T cells) did not associate
445 with positive patient outcomes, in keeping with T cell exhaustion constituting a profound

446 loss of T cell functionality [39]. This suggests that cells within subclusters 14–16 are critical in
447 mounting an effective anti-tumor response through mechanisms that sustain effector
448 function without succumbing to terminal exhaustion.
449
450 We next employed SCENIC analysis to highlight transcriptional regulatory systems that are
451 most pertinent to the functional and prognostic characteristics of these T cell populations
452 and revealed distinct regulatory patterns across the T cell subclusters, highlighting the
453 differential activity of several key transcription factors (**FIGURE 4H and SUPPLEMENTARY**
454 **FIGURE 3D)**. *Jdp2*, an AP-1 repressor, exhibited differential regulon activity across the T cell
455 subclusters, being elevated in subcluster 13 compared to subclusters 14-16. Higher *Jdp2*
456 expression contributes to impaired cellular functionality by T cell exhaustion and anergy
457 [40,41]. Therefore, lower activity of the *Jdp2* regulon in subclusters 14 and 15 is consistent
458 with a more functional and active T cell state and, considering the enrichment of these
459 subclusters with Combination treatment supports the notion that decreased *Jdp2* activity
460 facilitates better immune responses. Furthermore, elevated activity of the *Mxd1* regulon in
461 subcluster 13 suggests this, too, has a crucial role in maintaining the exhausted state
462 characteristic of this subcluster by repressing cellular growth, contributing to its adverse
463 clinical outcomes [42]. Antagonistic roles of *Mxd1* and *Myc* have been widely reported [43].
464 It is consistent, therefore, that the *Myc* regulon was notably active in T cell subclusters 14
465 and 15, whose signatures are linked to better prognoses. Elevated *Myc* activity in these
466 clusters indicates a role that supports T cell persistence and functionality, perhaps through
467 metabolic reprogramming and, when appropriate, proliferative activities that promote
468 favorable immune responses.
469

470 The findings from our cytotoxic T cell subclustering and gene expression analyses are further
471 supported by interrogation of bulk RNAseq data obtained from the YUMM2.1 subcutaneous
472 tumors described earlier. From our previous study, tumors from IFNγ pre-treated cells are
473 'immune deserts' and, in accordance, were characterized by a marked reduction in effector T
474 cell-associated signatures. In contrast, IgG-treated naïve tumors exhibited higher levels of T
475 cell activation and exhaustion, reflecting an active yet ultimately ineffective immune
476 response **(SUPPLEMENTARY FIGURE 3F)**. Interestingly, tumors relapsing on α-PD-1 therapy
477 displayed even higher levels of T cell activation and exhaustion than those treated with IgG
478 alone, which suggests that despite the robust initial immune response, these tumors
479 managed to evade sustained immune control. Conversely, α-PD-1 responding tumors
480 displayed lower levels of exhaustion and elevated markers of T cell hyperactivation,
481 consistent with a robust anti-tumor response. These bulk RNAseq findings align with our
482 scRNAseq data, indicating that Combination therapy may successfully replicate the T-cell
483 activation patterns seen in α-PD-1 responders. As the literature suggests activities that both
484 elicit pro-inflammatory responses and mediate tumor progression for hyperactivated T cells
485 [44,45], our TIDE analysis suggests the correlation with positive responses to α-PD-1 may be
486 transient and insufficient for long-term tumor control, emphasizing the need for more
487 durable therapeutic interventions.
488
489 To further explore the immune landscape shaped by Combination therapy, we performed a
490 flow cytometry analysis of α-PD-1 relapsing tumors treated with either α-PD-1 or
491 Combination therapy. Building on our observations of T cell dynamics, this revealed shifts in
492 T cell populations following Combination treatment compared to α-PD-1 treated tumors
493 **(SUPPLEMENTARY FIGURE 3G)**. Specifically, Combination treatment reduced expression of

494 GZMB by $CD8^+$ T cells, suggestive of a larger proportion of this cell type transitioned to the
495 quiescent state, as described previously in our scRNA-seq data. This shift was accompanied
496 by nuanced changes in the expression of immune checkpoint markers. We observed a
497 decrease in LAG-3 positivity among $PD\text{-}1^+$ $CD8^+$ T cells, indicative of reduced T cell
498 exhaustion and an enhancement of immune response. However, this was counterbalanced
499 by increased TIM-3 expression, another marker linked to T-cell dysfunction and exhaustion
500 [46,47]. Together, these findings highlight the complexity and heterogeneity of T cell states
501 in the TME that influence therapeutic efficacy.
502

503 **Combined α-PD-1 and PARP14 inhibitor treatment provokes dynamic immune evasion**
504 **strategies in tumor cells**

505 To further understand the impact of PARP14 inhibition on the TME, we further subclustered
506 tumor cells and Cancer-Associated Fibroblasts (CAFs)— covering clusters 26-28— into six
507 distinct subclusters (**FIGURE 5A and SUPPLEMENTARY TABLE 12**), representing key roles in
508 tumor progression and therapy adaptation. Among these, subcluster 3, identified as
509 differentiation-primed tumor cells, was markedly enriched by α-PD-1 monotherapy, with its
510 representation nearly doubling relative to IgG-treated tumors (**FIGURE 5B and C**). Slingshot
511 trajectory analysis [14] positioned subcluster 3 as the likely origin of hyper-proliferative
512 (subcluster 4) and immunomodulatory (subcluster 5) tumor states (**FIGURE 5D**). Gene Set
513 Enrichment Analysis (GSEA) confirmed an abundance of differentiation-linked pathways in
514 subcluster 3, suggesting that this state enhances susceptibility to immune-mediated
515 elimination (**FIGURE 5E**). Notably, the suppression of this cluster by combination therapy

516 underscores how targeting differentiation-associated vulnerabilities can limit tumor self-
517 renewal and survival pathways.
518
519 In contrast, tumor subclusters 1, 2, and 4 were enriched by Combination treatment.
520 Subcluster 2, characterized by highly invasive and adhesive tumor cells, drives metastasis via
521 extracellular matrix remodeling and, we infer, an adaptive response to evade immune attack
522 under intense therapeutic pressure, as evidenced by increased activation of biosynthetic
523 pathways (**FIGURE 5E**). Subcluster 1, defined by angiogenic and epithelial-mesenchymal
524 transition (EMT) phenotypes, enhances tumor migration, vascularization, and metastasis
525 while also dampening immune responses (**FIGURE 5E**). The metabolic activation observed in
526 subcluster 4 indicates an enhanced proliferative potential and cellular turnover under
527 treatment-induced stress, consistent with therapy-adapted, resistant tumor states. These
528 observations reveal distinct adaptive responses, including elevated angiogenesis, cell
529 expansion, and interference with immune cell recognition machinery (**FIGURE 5E**).
530 Therefore, while treatment suppresses key tumor-promoting pathways, it can also select
531 tumor adaptations that sustain tumor growth and permit immune escape despite the
532 pressure of combination therapy.
533
534 Integrative analysis of the top 200 DEGs across tumor subclusters allowed us to extract those
535 uniquely regulated in each subcluster, highlighting distinct transcriptional patterns
536 associated with therapeutic outcomes. By evaluating their expression in our YUMM2.1 bulk
537 tumor RNAseq data set, we observed that genes enriched in subclusters 1, 2, and 5
538 correlated with relapse following α-PD-1 monotherapy, whereas those from subclusters 3
539 and 4 were linked to initial therapeutic responses (**SUPPLEMENTARY FIGURE 5A**).

540

541 Analysis of these unique gene lists using TIDE largely corroborated our identification of
542 relapse or response outcomes. Subcluster 4, strongly associated with responders to α-PD-1
543 treatment in our data, was associated with improved patient survival **(SUPPLEMENTARY**
544 **FIGURE 5B and SUPPLEMENTARY TABLE 13).** In contrast, gene signatures linked to
545 subclusters relapsing on α-PD-1 therapy were predictive of worse clinical outcomes.
546 Interestingly, genes uniquely upregulated in subcluster 3 did not reliably predict clinical
547 response. This suggests that cells within this subcluster can adapt under selective pressure,
548 transitioning into states that are either vulnerable to immune attack or capable of immune
549 evasion. The dynamic interplay between these states ultimately shapes the overall
550 treatment outcome.

551

552 Evaluation of the PARP14i gene signature across subclusters revealed treatment- and
553 subcluster-specific regulation of key genes **(FIGURE 5F)**. Upregulation of many of these in
554 subcluster 1 by Combination therapy indicated elevated interferon signaling, while in
555 subcluster 4, their downregulation suggests reduced metabolic and proliferative activities. In
556 subcluster 3, α-PD-1 alone induced the PARP14i signature, but Combination therapy
557 tempered its upregulation, possibly to prevent chronic stimulation. In subcluster 2, PARP14
558 inhibition selectively reduced *Ifit3* while increasing *Gbp7,* indicating a shift towards Type II
559 interferon signaling.

560 **Discussion**

561 Current melanoma therapeutics, particularly immune checkpoint inhibitors (ICIs) such as α-
562 PD-1, have significantly advanced treatment, yet continue to face challenges from tumor
563 resistance. Although combination therapies and targeted agents have been explored, their
564 success in overcoming resistance mechanisms has been limited and necessitates novel
565 treatment intervention approaches to enhance therapeutic efficacy [48,49]. Our previous
566 research demonstrated PARP14 as a crucial regulator of immune responses, demonstrating
567 that its inhibition amplifies the activity of infiltrating T cells within the TME [5]. In this study,
568 we explore the effects of combining PARP14 inhibition with α-PD-1 therapy, to uncover the
569 role of PARP14 upon immune cell dynamics in the tumor immune infiltrate at the onset of α-
570 PD-1 resistance.

571

572 T cell exhaustion, marked by upregulation of inhibitory receptors and a reduction in cytokine
573 production and cytotoxic activity, is a central challenge in overcoming resistance [50,51]. Our
574 findings reveal that combining α-PD-1 with PARP14 inhibition mitigates T cell exhaustion by
575 inducing a hyperactivate T cell state which can progress to quiescence. Elevated expression
576 of genes associated with T cell hyperactivation contributes to a pro-inflammatory
577 environment which can control tumor growth [45], yet if excessive, instead exacerbates
578 tumor progression [44]. This implies an exit strategy, such as entering quiescence, preserves
579 T cell functionality, preventing terminal exhaustion while maintaining a reservoir of
580 reactivatable cells. These quiescent T cells, expressing longevity markers like *Bcl2* and *Il-6*,
581 contrast with classical exhaustion and may sustain anti-tumor immunity. Leveraging this
582 quiescent state could lead to durable responses by reactivating T cells with additional
583 therapies.

584

585 Contact between PILRA and CD8α has been shown to maintain cytotoxic T cells in a
586 quiescent state [52], presenting a potential axis for intervention. Moreover, *PILRA* expression
587 correlates with tumor immune infiltration and positive prognosis [53], suggesting its role in
588 preventing T cell exhaustion by promoting quiescence. Intriguingly, *Pilra* expression was
589 enhanced in M1-like macrophage subclusters (**FIGURE 3F)** enriched by Combination
590 treatment, supporting its role in inducing T cell quiescence. Notably, CD8α was highly
591 expressed in T cell subclusters 14 and 16 **(SUPPLEMENTARY FIGURE 3A)**, suggesting that
592 overcoming PILRA inhibition may be required to exit the quiescent state. While monoclonal
593 antibodies targeting PILRA have shown promise in preclinical models of autoinflammatory
594 diseases [54,55], their potential in cancer treatment remains unexplored. Targeting the
595 PILRA-CD8α axis therefore represents an appealing opportunity to enhance T cell-mediated
596 immunity when combined with existing therapies, promoting more active anti-tumor
597 responses.

598

599 In keeping with previous findings [7,8], we observed that PARP14 inhibition reshaped the
600 TME by reducing immunosuppressive signals, typically linked with TAMs, and fostering a pro-
601 inflammatory environment characterized by increased M1 macrophage polarization. TAMs
602 support tumor progression through tissue repair and immunosuppression [56,57], while M1
603 macrophages are instrumental in sustaining effective anti-tumor immune responses via
604 their production of pro-inflammatory cytokines such as TNF-α, IL-1β, and IL-6 [58,59].
605 Enriching M1 macrophages with PARP14i boosts cytokine and chemokine production,
606 enhancing the effectiveness of PD-1 blockade therapy by increasing the infiltration and
607 activation of cytotoxic T cells within the tumor [60,61]. Thus by enriching M1 macrophages,

608 PARP14 inhibition can amplify T cell activation and improve α-PD-1 therapy, offering a
609 potential strategy to overcome tumor immune evasion [62]. Together, the effects of PARP14
610 inhibition upon macrophages also likely contribute to counteracting T cell dysfunction often
611 associated with markers of ICI resistance, such as chronic IFNγ exposure.
612
613 PARP14 influences gene expression and chromatin remodeling via its interactions and
614 regulation of key immune pathways such as *STAT1* [8], *STAT3* [63], and *STAT6* [64] in co-
615 operation with histone deacetylases (HDACs). Recent studies highlight the critical role of
616 epigenetic regulation for macrophage polarization, whilst quiescent T cells actively manage
617 their epigenetic landscape to preserve their long-term functionality whilst remaining poised
618 for rapid reactivation [65]. We speculate that PARP14 inhibition disrupts the recruitment of
619 HDACs to these regions, thereby promoting a "dormant" memory state in both T cells and
620 macrophages. This state therefore requires further intervention to unlock the anti-tumor
621 potential of these immune cell states.
622
623 Our study revealed a robust PARP14 inhibition (PARP14i) gene signature that is strongly
624 associated with IFNγ signaling and STAT/IRF pathway regulation. While upregulated in α-PD-
625 1-treated samples, this signature did not differentiate treatment response from relapse in
626 our preclinical model. Nonetheless, high expression of the genes induced by PARP14i
627 correlates with improved patient survival. While combination therapy enhances T cell
628 activation and inflammation, it also induces expression changes amongst the PARP14i gene
629 signature, which, combined with mounting immune pressure, may simultaneously facilitate
630 the development of resistance mechanisms to allow tumor persistence. Notably, the
631 upregulation of *Stat1*, *Atf3*, *Irf1*, and *Cd274* in subcluster 1 suggests that combination

632 treatment may inadvertently enhance EMT-associated properties, thereby promoting more
633 invasive and immune-evasive tumor cells [66]. These highly dynamic adaptive resistance
634 mechanisms, therefore limit the promising effects our novel therapeutic combination upon
635 immune cells. This may explain why despite short-term control of tumor growth in
636 Combination therapy, these mechanisms later allow them to evade immunotherapy and
637 progress despite intensified immune pressure. Conversely, the downregulation of IFNγ-
638 regulated genes within the PARP14i signature in tumor subcluster 4 suggests reduced
639 intrinsic IFN signaling. This reduction could heighten the susceptibility of these highly
640 proliferative tumor cells to immune-mediated destruction [67]. This observation highlights
641 the remarkable adaptability within the TME and aligns with findings from other studies that
642 have reported similar resistance-associated tumor dynamics in response to targeted
643 therapies [68,69].
644
645 The observed adaptive resistance underscores the necessity for a multifaceted approach to
646 cancer treatment. While combining α-PD-1 therapy with PARP14 inhibition initially shows
647 promise, rapid evolution of adaptive resistance mechanisms remains a considerable
648 concern. To address this challenge, future research should focus on multi-modal strategies
649 that integrate immune checkpoint inhibitors with agents that enhance pro-inflammatory
650 immune infiltrates to produce a robust and durable anti-tumor response. Moreover, our
651 identification of a PARP14i gene signature offers therapeutic promise, particularly for
652 patients with low expression of these genes, enabling a more personalized treatment
653 strategy. By using this signature as a biomarker, therapy can be tailored to individual patients
654 in order to optimize treatment outcomes and minimize unnecessary interventions in
655 patients who are less likely to respond. Further refinement should focus upon identifying

656 complementary interventions to apply alongside the combination therapy that prevents
657 tumor cells from evading immune detection or restores T cell-APC interactions to increase
658 their tumor killing capacity. With continued research into resistance mechanisms and
659 alternative pathways, robust combination therapies can potentially be developed which
660 overcome even the most resilient tumor populations, offering a path toward more durable,
661 comprehensive responses and improved patient survival.

662 **Declarations**

663 **Acknowledgments**

664 This study was funded by a research sponsorship agreement between Ribon Therapeutics
665 and The University of Manchester, grant 821034 from the Melanoma Research Alliance
666 (MRA), grant 22-0091 from Worldwide Cancer Research (WCR), and an award from the Skin
667 Cancer Research Fund (SCaRF). C.W.W. was funded by a scholarship from the Hong Kong
668 Scholarship for Excellence Scheme (HKSES). We thank Dr Gareth Howell and The University
669 of Manchester Flow Cytometry Core Facility for facilitating flow cytometry analysis, Dr Andy
670 Hayes and Claire Morrisroe in the Genomic Technologies Core Facility for assistance with
671 single-cell RNA sequencing, Dr Leo Zeef and the Bioinformatics Core facility for their help
672 with bioinformatic analysis, and members of the Biological Services Facility at The University
673 of Manchester for help with animal work. FIGURE 2A and Graphical Abstract were created
674 using BioRender.

675

676 **Author Contributions Statement**

677 A.H. conceived the study. R.L., K.N.S., and C.W.W. performed experiments. I.L. and R.L.
678 analyzed the scRNAseq data. K.N.S. analyzed the flow cytometry and bulk RNAseq data.
679 D.T.I., M.N., and A.H. contributed to experimental design and data analysis. R.L., K.N.S., and
680 A.H. drafted the original version of this manuscript, with all authors reviewing subsequent
681 drafts. A.H. obtained funding for the study.

682

683 **Competing Interests Statement**

684 The authors declare the following competing interests:

D.T.I. and M.N. were employees and shareholders of Ribon Therapeutics at the time of data collection. A.H. received research sponsorship from Ribon Therapeutics. All other authors declare no competing interests.

690 **References**

691 [1] Ribas A, Hamid O, Daud A, Hodi FS, Wolchok JD, Kefford R, et al. Association of
692 Pembrolizumab With Tumor Response and Survival Among Patients With Advanced
693 Melanoma. JAMA 2016;315:1600. https://doi.org/10.1001/jama.2016.4059.
694 [2] Lim J, Kang I, La J, Ku KB, Kang BH, Kim Y, et al. Harnessing type I interferon-mediated
695 immunity to target malignant brain tumors. Front Immunol 2023;14:1203929.
696 https://doi.org/10.3389/fimmu.2023.1203929.
697 [3] Qiu J, Xu B, Ye D, Ren D, Wang S, Benci JL, et al. Cancer cells resistant to immune
698 checkpoint blockade acquire interferon-associated epigenetic memory to sustain T cell
699 dysfunction. Nat Cancer 2023. https://doi.org/10.1038/s43018-022-00490-y.
700 [4] Benci JL, Johnson LR, Choa R, Xu Y, Qiu J, Zhou Z, et al. Opposing Functions of Interferon
701 Coordinate Adaptive and Innate Immune Responses to Cancer Immune Checkpoint
702 Blockade. Cell 2019;178:933-948.e14. https://doi.org/10.1016/j.cell.2019.07.019.
703 [5] Wong CW, Evangelou C, Sefton KN, Leshem R, Zhang W, Gopalan V, et al. PARP14
704 inhibition restores PD-1 immune checkpoint inhibitor response following IFNγ-driven
705 acquired resistance in preclinical cancer models. Nat Commun 2023;14:5983.
706 https://doi.org/10.1038/s41467-023-41737-1.
707 [6] Meeth K, Wang JX, Micevic G, Damsky W, Bosenberg MW. The YUMM lines: a series of
708 congenic mouse melanoma cell lines with defined genetic alterations. Pigment Cell
709 Melanoma Res 2016;29:590–7. https://doi.org/10.1111/pcmr.12498.
710 [7] Schenkel LB, Molina JR, Swinger KK, Abo R, Blackwell DJ, Lu AZ, et al. A potent and
711 selective PARP14 inhibitor decreases protumor macrophage gene expression and elicits
712 inflammatory responses in tumor explants. Cell Chem Biol 2021;28:1158-1168.e13.
713 https://doi.org/10.1016/j.chembiol.2021.02.010.
714 [8] Iwata H, Goettsch C, Sharma A, Ricchiuto P, Goh WWB, Halu A, et al. PARP9 and PARP14
715 cross-regulate macrophage activation via STAT1 ADP-ribosylation. Nat Commun
716 2016;7:12849. https://doi.org/10.1038/ncomms12849.
717 [9] Caprara G, Prosperini E, Piccolo V, Sigismondo G, Melacarne A, Cuomo A, et al. PARP14
718 Controls the Nuclear Accumulation of a Subset of Type I IFN–Inducible Proteins. J
719 Immunol 2018;200:2439–54. https://doi.org/10.4049/jimmunol.1701117.
720 [10] Wigle TJ, Ren Y, Molina JR, Blackwell DJ, Schenkel LB, Swinger KK, et al. Targeted
721 Degradation of PARP14 Using a Heterobifunctional Small Molecule. ChemBioChem
722 2021;22:2107–10. https://doi.org/10.1002/cbic.202100047.
723 [11] Amezquita RA, Lun ATL, Becht E, Carey VJ, Carpp LN, Geistlinger L, et al. Orchestrating
724 single-cell analysis with Bioconductor. Nat Methods 2020;17:137–45.
725 https://doi.org/10.1038/s41592-019-0654-x.
726 [12] Zhou Y, Zhou B, Pache L, Chang M, Khodabakhshi AH, Tanaseichuk O, et al. Metascape
727 provides a biologist-oriented resource for the analysis of systems-level datasets. Nat
728 Commun 2019;10:1523. https://doi.org/10.1038/s41467-019-09234-6.
729 [13] Blondel VD, Guillaume J-L, Lambiotte R, Lefebvre E. Fast unfolding of communities in
730 large networks. J Stat Mech Theory Exp 2008;2008:P10008.
731 https://doi.org/10.1088/1742-5468/2008/10/P10008.
732 [14] Street K, Risso D, Fletcher RB, Das D, Ngai J, Yosef N, et al. Slingshot: cell lineage and
733 pseudotime inference for single-cell transcriptomics. BMC Genomics 2018;19:477.
734 https://doi.org/10.1186/s12864-018-4772-0.

[15] Fu J, Li K, Zhang W, Wan C, Zhang J, Jiang P, et al. Large-scale public data reuse to model immunotherapy response and resistance. Genome Med 2020;12:21. https://doi.org/10.1186/s13073-020-0721-z.

[16] Andreatta M, Corria-Osorio J, Müller S, Cubas R, Coukos G, Carmona SJ. Interpretation of T cell states from single-cell transcriptomics data using reference atlases. Nat Commun 2021;12:2965. https://doi.org/10.1038/s41467-021-23324-4.

[17] Higashi H, Maejima T, Lee LH, Yamazaki Y, Hottiger MO, Singh SA, et al. A Study into the ADP-Ribosylome of IFN-γ-Stimulated THP-1 Human Macrophage-like Cells Identifies ARTD8/PARP14 and ARTD9/PARP9 ADP-Ribosylation. J Proteome Res 2019;18:1607–22. https://doi.org/10.1021/acs.jproteome.8b00895.

[18] Lachmann A, Torre D, Keenan AB, Jagodnik KM, Lee HJ, Wang L, et al. Massive mining of publicly available RNA-seq data from human and mouse. Nat Commun 2018;9:1366. https://doi.org/10.1038/s41467-018-03751-6.

[19] Nathanson T, Ahuja A, Rubinsteyn A, Aksoy BA, Hellmann MD, Miao D, et al. Somatic Mutations and Neoepitope Homology in Melanomas Treated with CTLA-4 Blockade. Cancer Immunol Res 2017;5:84–91. https://doi.org/10.1158/2326-6066.CIR-16-0019.

[20] Mariathasan S, Turley SJ, Nickles D, Castiglioni A, Yuen K, Wang Y, et al. TGFβ attenuates tumour response to PD-L1 blockade by contributing to exclusion of T cells. Nature 2018;554:544–8. https://doi.org/10.1038/nature25501.

[21] Gide TN, Quek C, Menzies AM, Tasker AT, Shang P, Holst J, et al. Distinct Immune Cell Populations Define Response to Anti-PD-1 Monotherapy and Anti-PD-1/Anti-CTLA-4 Combined Therapy. Cancer Cell 2019;35:238-255.e6. https://doi.org/10.1016/j.ccell.2019.01.003.

[22] Wang X, Qiu L, Li Z, Wang X-Y, Yi H. Understanding the Multifaceted Role of Neutrophils in Cancer and Autoimmune Diseases. Front Immunol 2018;9. https://doi.org/10.3389/fimmu.2018.02456.

[23] Sturniolo I, Váróczy C, Regdon Z, Mázló A, Muzsai S, Bácsi A, et al. PARP14 Contributes to the Development of the Tumor-Associated Macrophage Phenotype. Int J Mol Sci 2024;25:3601. https://doi.org/10.3390/ijms25073601.

[24] Nasrollahzadeh E, Razi S, Keshavarz-Fathi M, Mazzone M, Rezaei N. Pro-tumorigenic functions of macrophages at the primary, invasive and metastatic tumor site. Cancer Immunol Immunother CII 2020;69:1673–97. https://doi.org/10.1007/s00262-020-02616-6.

[25] Zhou Y, Guo L, Sun H, Xu J, Ba T. CXCR5+ CD8 T cells displayed higher activation potential despite high PD-1 expression, in tumor-involved lymph nodes from patients with thyroid cancer. Int Immunopharmacol 2018;62:114–9. https://doi.org/10.1016/j.intimp.2018.07.002.

[26] Bai M, Zheng Y, Liu H, Su B, Zhan Y, He H. CXCR5+ CD8+ T cells potently infiltrate pancreatic tumors and present high functionality. Exp Cell Res 2017;361:39–45. https://doi.org/10.1016/j.yexcr.2017.09.039.

[27] Hussain M, Liu J, Wang G-Z, Zhou G-B. CXCL13 Signaling in the Tumor Microenvironment. In: Birbrair A, editor. Tumor Microenviron., vol. 1302, Cham: Springer International Publishing; 2021, p. 71–90. https://doi.org/10.1007/978-3-030-62658-7_6.

[28] Korbecki J, Bosiacki M, Barczak K, Łagocka R, Chlubek D, Baranowska-Bosiacka I. The Clinical Significance and Role of CXCL1 Chemokine in Gastrointestinal Cancers. Cells 2023;12:1406. https://doi.org/10.3390/cells12101406.

782 [29] Liu Y, Cai Y, Liu L, Wu Y, Xiong X. Crucial biological functions of CCL7 in cancer. PeerJ
783 2018;6:e4928. https://doi.org/10.7717/peerj.4928.
784 [30] Kloc M, Kubiak JZ, Zdanowski R, Ghobrial RM. Memory Macrophages. Int J Mol Sci
785 2022;24:38. https://doi.org/10.3390/ijms24010038.
786 [31] Liu Z, Kuang W, Zhou Q, Zhang Y. TGF-β1 secreted by M2 phenotype macrophages
787 enhances the stemness and migration of glioma cells via the SMAD2/3 signalling
788 pathway. Int J Mol Med 2018;42:3395. https://doi.org/10.3892/ijmm.2018.3923.
789 [32] Sestito C, Brevé JJP, Bol JGJM, Wilhelmus MMM, Drukarch B, van Dam A-M. Tissue
790 Transglutaminase contributes to myelin phagocytosis in interleukin-4-treated human
791 monocyte-derived macrophages. Cytokine 2020;128:155024.
792 https://doi.org/10.1016/j.cyto.2020.155024.
793 [33] Aibar S, González-Blas CB, Moerman T, Huynh-Thu VA, Imrichova H, Hulselmans G, et al.
794 SCENIC: single-cell regulatory network inference and clustering. Nat Methods
795 2017;14:1083–6. https://doi.org/10.1038/nmeth.4463.
796 [34] Mehrotra P, Hollenbeck A, Riley JP, Li F, Patel RJ, Akhtar N, et al. Poly (ADP-ribose)
797 polymerase 14 and its enzyme activity regulates TH2 differentiation and allergic airway
798 disease. J Allergy Clin Immunol 2013;131:521-531.e12.
799 https://doi.org/10.1016/j.jaci.2012.06.015.
800 [35] Cho SH, Raybuck A, Wei M, Erickson J, Nam KT, Cox RG, et al. B Cell–Intrinsic and –
801 Extrinsic Regulation of Antibody Responses by PARP14, an Intracellular (ADP-
802 Ribosyl)Transferase. J Immunol 2013;191:3169–78.
803 https://doi.org/10.4049/jimmunol.1301106.
804 [36] Sun L, Su Y, Jiao A, Wang X, Zhang B. T cells in health and disease. Signal Transduct
805 Target Ther 2023;8:235. https://doi.org/10.1038/s41392-023-01471-y.
806 [37] Choi H, Song H, Jung YW. The Roles of CCR7 for the Homing of Memory CD8+ T Cells
807 into Their Survival Niches. Immune Netw 2020;20:e20.
808 https://doi.org/10.4110/in.2020.20.e20.
809 [38] Vilgelm AE, Richmond A. Chemokines Modulate Immune Surveillance in Tumorigenesis,
810 Metastasis, and Response to Immunotherapy. Front Immunol 2019;10:333.
811 https://doi.org/10.3389/fimmu.2019.00333.
812 [39] Wherry EJ, Kurachi M. Molecular and cellular insights into T cell exhaustion. Nat Rev
813 Immunol 2015;15:486–99. https://doi.org/10.1038/nri3862.
814 [40] Yuanhong X, Feng X, Qingchang L, Jianpeng F, Zhe L, Kejian G. Downregulation of Ap-1
815 Repressor Jdp2 is Associated with Tumor Metastasis and Poor Prognosis in Patients
816 with Pancreatic Carcinoma. Int J Biol Markers 2010;25:136–40.
817 https://doi.org/10.1177/172460081002500303.
818 [41] Atsaves V, Leventaki V, Rassidakis GZ, Claret FX. AP-1 Transcription Factors as Regulators
819 of Immune Responses in Cancer. Cancers 2019;11:1037.
820 https://doi.org/10.3390/cancers11071037.
821 [42] Iritani BM, Delrow J, Grandori C, Gomez I, Klacking M, Carlos LS, et al. Modulation of T-
822 lymphocyte development, growth and cell size by the Myc antagonist and
823 transcriptional repressor Mad1. EMBO J 2002;21:4820.
824 https://doi.org/10.1093/emboj/cdf492.
825 [43] Lüscher B. MAD1 and its life as a MYC antagonist: An update. Eur J Cell Biol
826 2012;91:506–14. https://doi.org/10.1016/j.ejcb.2011.07.005.

827 [44] Kalfaoglu B, Almeida-Santos J, Tye CA, Satou Y, Ono M. T-Cell Hyperactivation and
828 Paralysis in Severe COVID-19 Infection Revealed by Single-Cell Analysis. Front Immunol
829 2020;11. https://doi.org/10.3389/fimmu.2020.589380.
830 [45] Palmer DC, Webber BR, Patel Y, Johnson MJ, Kariya CM, Lahr WS, et al. Internal
831 checkpoint regulates T cell neoantigen reactivity and susceptibility to PD1 blockade.
832 Med 2022;3:682-704.e8. https://doi.org/10.1016/j.medj.2022.07.008.
833 [46] Avery L, Filderman J, Szymczak-Workman AL, Kane LP. Tim-3 co-stimulation promotes
834 short-lived effector T cells, restricts memory precursors, and is dispensable for T cell
835 exhaustion. Proc Natl Acad Sci 2018;115:2455–60.
836 https://doi.org/10.1073/pnas.1712107115.
837 [47] Minnie SA, Waltner OG, Zhang P, Takahashi S, Nemychenkov NS, Ensbey KS, et al. TIM-
838 3+ CD8 T cells with a terminally exhausted phenotype retain functional capacity in
839 hematological malignancies. Sci Immunol 2024;9:eadg1094.
840 https://doi.org/10.1126/sciimmunol.adg1094.
841 [48] Huang AC, Zappasodi R. A decade of checkpoint blockade immunotherapy in
842 melanoma: understanding the molecular basis for immune sensitivity and resistance.
843 Nat Immunol 2022;23:660–70. https://doi.org/10.1038/s41590-022-01141-1.
844 [49] Rager T, Eckburg A, Patel M, Qiu R, Gantiwala S, Dovalovsky K, et al. Treatment of
845 Metastatic Melanoma with a Combination of Immunotherapies and Molecularly
846 Targeted Therapies. Cancers 2022;14:3779. https://doi.org/10.3390/cancers14153779.
847 [50] Wherry EJ, Kurachi M. Molecular and cellular insights into T cell exhaustion. Nat Rev
848 Immunol 2015;15:486–99. https://doi.org/10.1038/nri3862.
849 [51] Collier JL, Weiss SA, Pauken KE, Sen DR, Sharpe AH. Not-so-opposite ends of the
850 spectrum: CD8+ T cell dysfunction across chronic infection, cancer and autoimmunity.
851 Nat Immunol 2021;22:809–19. https://doi.org/10.1038/s41590-021-00949-7.
852 [52] Zheng L, Han X, Yao S, Zhu Y, Klement J, Wu S, et al. The CD8α-PILRα interaction
853 maintains CD8+ T cell quiescence. Science 2022;376:996–1001.
854 https://doi.org/10.1126/science.aaz8658.
855 [53] Li Q, Yang Z, He X, Yang X. Comprehensive analysis of PILRA's association with the
856 prognosis, tumor immune infiltration, and immunotherapy in pan-cancer. Sci Rep
857 2023;13:14334. https://doi.org/10.1038/s41598-023-41649-6.
858 [54] Sun Y, Caplazi P, Zhang J, Mazloom A, Kummerfeld S, Quinones G, et al. PILRα
859 Negatively Regulates Mouse Inflammatory Arthritis. J Immunol 2014;193:860–70.
860 https://doi.org/10.4049/jimmunol.1400045.
861 [55] Monroe K, Weerakkody T, Sabelström H, Tatarakis D, Suh J, Chin M, et al. PILRA
862 regulates microglial neuroinflammation and lipid metabolism as a candidate
863 therapeutic target for Alzheimer's disease 2024. https://doi.org/10.21203/rs.3.rs-
864 3954863/v1.
865 [56] Wang H, Yung MMH, Ngan HYS, Chan KKL, Chan DW. The Impact of the Tumor
866 Microenvironment on Macrophage Polarization in Cancer Metastatic Progression. Int J
867 Mol Sci 2021;22:6560. https://doi.org/10.3390/ijms22126560.
868 [57] Chen S, Saeed AFUH, Liu Q, Jiang Q, Xu H, Xiao GG, et al. Macrophages in
869 immunoregulation and therapeutics. Signal Transduct Target Ther 2023;8:207.
870 https://doi.org/10.1038/s41392-023-01452-1.
871 [58] Sica A, Erreni M, Allavena P, Porta C. Macrophage polarization in pathology. Cell Mol
872 Life Sci 2015;72:4111–26. https://doi.org/10.1007/s00018-015-1995-y.

[59] Mantovani A, Marchesi F, Malesci A, Laghi L, Allavena P. Tumour-associated macrophages as treatment targets in oncology. Nat Rev Clin Oncol 2017;14:399–416. https://doi.org/10.1038/nrclinonc.2016.217.
[60] Zhang Y, Guan X, Jiang P. Cytokine and Chemokine Signals of T-Cell Exclusion in Tumors. Front Immunol 2020;11. https://doi.org/10.3389/fimmu.2020.594609.
[61] Kohli K, Pillarisetty VG, Kim TS. Key chemokines direct migration of immune cells in solid tumors. Cancer Gene Ther 2022;29:10–21. https://doi.org/10.1038/s41417-021-00303-x.
[62] Qian B-Z, Pollard JW. Macrophage Diversity Enhances Tumor Progression and Metastasis. Cell 2010;141:39–51. https://doi.org/10.1016/j.cell.2010.03.014.
[63] Mehrotra P, Krishnamurthy P, Sun J, Goenka S, Kaplan MH. Poly-ADP-ribosyl polymerase-14 promotes T helper 17 and follicular T helper development. Immunology 2015;146:537–46. https://doi.org/10.1111/imm.12515.
[64] Mehrotra P, Riley JP, Patel R, Li F, Voss L, Goenka S. PARP-14 Functions as a Transcriptional Switch for Stat6-dependent Gene Activation. J Biol Chem 2011;286:1767–76. https://doi.org/10.1074/jbc.M110.157768.
[65] Bennett TJ, Udupa VAV, Turner SJ. Running to Stand Still: Naive CD8+ T Cells Actively Maintain a Program of Quiescence. Int J Mol Sci 2020;21:9773. https://doi.org/10.3390/ijms21249773.
[66] Liu Z, Yu X, Xu L, Li Y, Zeng C. Current insight into the regulation of PD-L1 in cancer. Exp Hematol Oncol 2022;11:44. https://doi.org/10.1186/s40164-022-00297-8.
[67] Castro F, Cardoso AP, Gonçalves RM, Serre K, Oliveira MJ. Interferon-Gamma at the Crossroads of Tumor Immune Surveillance or Evasion. Front Immunol 2018;9. https://doi.org/10.3389/fimmu.2018.00847.
[68] Anderson KG, Stromnes IM, Greenberg PD. Obstacles Posed by the Tumor Microenvironment to T cell Activity: A Case for Synergistic Therapies. Cancer Cell 2017;31:311–25. https://doi.org/10.1016/j.ccell.2017.02.008.
[69] Yang L, Li A, Lei Q, Zhang Y. Tumor-intrinsic signaling pathways: key roles in the regulation of the immunosuppressive tumor microenvironment. J Hematol OncolJ Hematol Oncol 2019;12:125. https://doi.org/10.1186/s13045-019-0804-8.

906 **Figure Legends**

907 **Figure 1 – Identification of a genetic signature associated with PARP14 inhibition.**
908 YUMM2.1 and 501MEL cells treated for 48h *in vitro* with either DMSO, 100nM PARP14
909 inhibitor (RBN012759), or 500nM PARP14 PROTAC (RBN012811); *n* = 3. **A.** Bulk RNAseq
910 analysis of a PARP14 inhibition signature identified across human and mouse cell lines.
911 Heatmap of treatment vs control per cell line, colors representing row-scaled z-score
912 expression high (red) to low (blue). **B.** Gene set enrichment analysis (GSEA) of 30 PARP14i
913 signature genes identified by comparison of bulk RNAseq from human and mouse cell lines,
914 chronically treated with IFN-γ followed by 48 hours of PARP14 inhibition (Metascape
915 analysis, values presented as -$\log_{10}$ of P value). **C.** Kaplan-Meier (KM) curves showing cancer
916 patients with high Tumor Immune Dysfunction and Exclusion (TIDE) scores of PARP14i
917 signature genes having better overall survival (OS) rates in representative studies. Red
918 indicates patients with high (top 50%) TIDE scores and blue indicates low (bottom 50%) TIDE
919 scores. **D.** Bulk RNAseq analysis on naïve YUMM2.1 tumors treated with IgG or α-PD-1. α-
920 PD-1-treated cohort was split into relapsed (REL) and responders (RES). Compared to
921 YUMM2.1 tumors pre-treated with chronic IFN-γ stimulation.
922
923 **Figure 2 – Analysis of the cellular composition of YUMM2.1 tumors relapsing following α-**
924 **PD-1 antibodies with and without PARP14 inhibitor treatment**.
925 **A.** YUMM2.1 cells were implanted subcutaneously into the flank of female C57BL/6 mice.
926 Once tumors reached ~80mm^3 in volume, treatment of α-PD-1 antibodies was commenced
927 for a total of two doses, 3 days apart. Tumor shrinkage and regrowth was monitored. When
928 tumors reached a volume between ~100-150mm^3, a second round of treatment
929 commenced, lasting 7 days. Tumors were subsequently processed for single-cell RNAseq.
930 Graphical summary of experimental timeline, showing tumor inoculation and treatment
931 regime (top), and illustration of tumor growth (bottom). Created in BioRender. Leshem, R.
932 (2023) BioRender.com/r18g555. **B.** Mutual nearest neighbor (MNN) corrected Uniform
933 Manifold Approximation and Projection (UMAP) of 13 tumor samples (*n*=65,476 cells).
934 Clustered using Leiden unsupervised clustering and colored by cell types. Cluster identifies
935 below. **C.** Cell number changes in each cluster by treatment: three mice IgG2a; three mice α-
936 PD-1; three mice PARP14i (RBN012759) alone; and four mice a combination of α-PD-1 +
937 PARP14i (RBN012759). **D.** Cell density projections by treatment.
938
939 **Figure 3 - PARP14 inhibitor treatment increases M1 macrophage polarization to generate a**
940 **memory-like state.**
941 **A.** MNN corrected UMAP of monocytes and macrophages (clusters 1-8 of main data,
942 *n*=34,705). Subclustered using Louvain method of community ordering and colored by
943 subclusters. **B.** Cell number changes in each subcluster by treatment: IgG2a; α-PD-1; PARP14i
944 (RBN012759); combination treatment α-PD-1 + PARP14i (RBN012759). **C.** Cell density
945 projections of both monocytes and macrophages (colloquially referred to as MonoMacs) by
946 treatment. **D.** Macrophage subcluster identity- subclusters 2, 4, 8 and 10. GSEA of up-
947 (FDR=0.05, logFC > 1, marked in red) and downregulated (FDR=0.05, logFC < -1, marked in
948 blue) genes (Metascape analysis, values presented as -$\log_{10}$ of P value). **E.** Cytokine and
949 Chemokine gene expression presented as high (red) to low (blue) average expression and
950 ratio of cells expressing (circle size), across Macrophage subclusters. **F.** Gene expression
951 presented as high (red) to low (blue) average expression and ratio of cells expressing (circle

size), across Macrophage subclusters in different treatments. **G.** Binarized heatmap of 10% random subsampling of each MonoMac subcluster by relative regulon activity (SCENIC analysis).

Figure 4 - PARP14 inhibitor treatment in combination with α-PD-1 therapy drives activated cytotoxic T cells but limits transition to dysfunctional states.
A. MNN corrected UMAP of T cell and natural killer (NK) cells (clusters 12-17 main data, *n=18,298*). Subclustered using Louvain method of community ordering and colored by subclusters. **B.** Cell number changes in each T and NK cell subcluster by treatment: IgG2a; α-PD-1; PARP14i (RBN012759); combination treatment α-PD-1 + PARP14i (RBN012759). **C.** Cell density projections of T and NK cells by treatment. **D.** Cytokine and Chemokine gene expression presented as high (red) to low (blue) average expression and ratio of cells expressing (circle size), across T and NK cell subclusters. **E.** T cell subcluster identity- clusters 13-16. GSEA relevant terms of up- (red, FDR=0.05, top 25 genes) and downregulated (blue, FDR=0.05, bottom 25 genes) genes (Metascape analysis, values presented as $-\log_{10}$ of P value). **F.** Slingshot trajectory inference analysis of $CD8^+$ T cell subclusters 13-18 (*n=6,194*) with trajectory direction indicated by arrows (black). **G.** KM curves showing cancer patients with high TIDE scores of genes from T cell subclusters 13-16 and their effect on OS rates in bladder cancer cohort. Red indicates patients with high (top 50%) TIDE scores and blue indicates low (bottom 50%) TIDE scores. **H.** Binarized heatmap of each T cell subcluster by relative regulon activity (SCENIC analysis).

Figure 5 - Combined treatment of α-PD-1 with PARP14 inhibitor promotes dynamic adaptive resistance strategies in tumor cells which permit their persistence.
A. MNN corrected UMAP of tumor and cancer associated fibroblasts (CAFs) cells (clusters 26-28, *n=3,445*). Subclustered using Louvain method of community ordering and colored by subclusters. **B.** Cell number changes in each subcluster by treatment: IgG2a; α-PD-1; PARP14i (RBN012759); combination treatment α-PD-1 + PARP14i (RBN012759). **C.** Cell density projections of tumor and CAF cells by treatment. **D.** Slingshot trajectory inference analysis of tumor cells with trajectory direction indicated by arrows (black). **E.** Tumor subcluster identity, GSEA relevant terms of up- (red, FDR=0.05, logFC > 1) and downregulated (blue, FDR=0.05, logFC < -1) genes in tumor subclusters 1-4 (Metascape analysis, values presented as $-\log_{10}$ of P value). **F.** PARP14i signature gene expression presented as high (red) to low (blue) average expression and ratio of cells expressing (circle size), across tumor and CAF subclusters in different treatments. **G.** Cytokine and Chemokine gene expression presented as high (red) to low (blue) average expression and ratio of cells expressing (circle size), across Tumor and CAF subclusters.

993 **Supplementary Figure Legends**

994

995 **Supplementary Figure 1 – Identification of a genetic signature associated with PARP14**
996 **inhibition.**
997 **A.** MC38 or A375 cells treated for 48h *in vitro* with either DMSO, 100nM PARP14 inhibitor
998 (RBN012759), or 500nM PARP14 PROTAC (RBN012811); *n* = 3. Bulk RNAseq analysis of a
999 PARP14 inhibition signature identified across human and mouse cell lines. Heatmap of
1000 treatment vs control per cell line, colors representing row-scaled z-score expression high
1001 (red) to low (blue). **B.** Clustergram of gene-TF associations derived from EnrichR analysis
1002 using the ARCHS4_TFs_Coexp database. Heatmap displays associations between genes
1003 (rows) and transcription factor terms (columns). Color-coded to represent the -log10
1004 transformed adjusted p-values of enrichment, darker colors indicating stronger statistical
1005 significance. No normalization is applied, ensuring raw association strengths are visualized.
1006

1007 **Supplementary Figure 2 -**
1008 **A.** YUMM2.1 cells were implanted subcutaneously into the flank of female C57BL/6 mice.
1009 Once tumors reached ~80mm^3 in volume, treatment of α-PD-1 antibodies was commenced
1010 for a total of two doses, 3 days apart (horizontal dotted line). Tumor shrinkage and regrowth
1011 was monitored and individual growth curves plotted. When tumors reached a volume
1012 between ~100-150mm^3, a second round of treatment commenced (day 0); consisting of four
1013 IgG2a, α-PD-1, PARP14i or a combination of α-PD-1 + PARP14i. Treatment lasted 7 days.
1014 Tumors were subsequently excised and processed for single-cell RNAseq. **B.** RNAseq data of
1015 excluded IgG2a control treated tumor sample RL11i (black triangles and high-density lines)
1016 projected on the sample UMAP (color) using projecTILs R package. **C.** Sample representation
1017 in each cluster **–** histogram and **D.** UMAP. **E.** Cell number changes in each cell type by
1018 treatment: three mice IgG2a; three mice α-PD-1; three mice PARP14i (RBN012759) alone;
1019 and four mice a combination of α-PD-1 + PARP14i (RBN012759).
1020

1021 **Supplementary Figure 3-**
1022 **A.** Selected T cell marker gene expression presented as high (red) to low (blue) average
1023 expression and ratio of cells expressing (circle size), across T cell subclusters. **B.** Bulk RNAseq
1024 analysis on naïve YUMM2.1 tumors treated with IgG or α-PD-1. α-PD-1-treated cohort was
1025 split into relapsed (REL) and responders (RES). Compared to YUMM2.1 tumors pre-treated
1026 with chronic IFN-γ stimulation. Heatmap representations of activation and exhaustion
1027 markers. **C.** Gene expression presented as high (red) to low (blue) average expression and
1028 ratio of cells expressing (circle size), across T cell subclusters 13-16. **D.** Binarized heatmap of
1029 CD8+ T cell subclusters in Jdp2, Myc and Mxd1 regulons by relative regulon activity (SCENIC
1030 analysis). **E.** KM curves showing cancer patients with high TIDE scores of genes from T cell
1031 subclusters 13-16 and their effect on OS rates in bladder cancer cohort. Red indicates
1032 patients with high (top 50%) TIDE scores and blue indicates low (bottom 50%) TIDE scores.
1033 **F.** Representative image of Arid3a, Cebpb, Irf5, Mxd1 regulon activity AUC score in MNN
1034 corrected T cell subcluster UMAP. Calculated by SCENIC. **G.** Flow cytometry analysis of
1035 YUMM2.1 tumor xenografts in C57BL/6 mice relapsing on an initial dose of α-PD-1 and
1036 harvested on-treatment following subsequent dosing with either α-PD-1 (Blue; *n* = 6) or α-
1037 PD-1 + PARP14i (Red; *n* = 6). **From left to right:** Percentage of total immune cells and
1038 individual T cell subsets as a proportion of CD45$^+$ cells. Percentage of cytotoxic CD8$^+$ T cells

evaluated via their expression of GZMB. Percentage of exhaustion subsets in cytotoxic T cells measured by LAG-3 and TIM-3 levels for PD-1^{+}, PD-1^{+}CTLA-4^{+}, or PD-1^{+}CTLA-4^{-} background. The p-value was assessed by two-sided unpaired t-test and the data were presented as the mean ± SEM. *$p < 0.05$, ***$p < 0.01$, ***$p < 0.001$, ****$p < 0.0001$.

Supplementary Figure 4 – Flow cytometry gating strategy for T cell subsets and exhaustion phenotypes

Supplementary Figure 5 –
A. Bulk RNAseq analysis on naïve YUMM2.1 tumors treated with IgG or α-PD-1. α-PD-1-treated cohort was split into relapsed and responders. Compared to YUMM2.1 tumors pre-treated with chronic IFN-γ stimulation. Heatmap representations of uniquely upregulated genes per each subcluster within the top 200 expressed genes. Boxes represent relevant clinical outcome per cluster. **B.** KM curves showing cancer patients with high TIDE scores of uniquely upregulated genes per tumor subcluster and their effect on OS rates in bladder cancer cohort. Red indicates patients with high (top 50%) TIDE scores and blue indicates low (bottom 50%) TIDE scores.

Supplementary Tables

Supplementary Table 1: Gene Signatures
Supplementary Table 2: Tumor Size
Supplementary Table 3: Sample Identity
Supplementary Table 4: Cell Number Per Sample
Supplementary Table 5: Cluster Identity
Supplementary Table 6: Cell Number Per Cluster
Supplementary Table 7: Expression of Manually Selected Genes
Supplementary Table 8: Top 100 Expressed Genes Per Cluster – Main
Supplementary Table 9: Top 100 Expressed Genes Per Cluster - NK and T Cells
Supplementary Table 10: Top 25 Genes Up / Down Regulated in T Cell Clusters 13-16
Supplementary Table 11: Top 100 Expressed Genes Per Cluster - Mono / Macs
Supplementary Table 12: Top 100 Expressed Genes Per Cluster - Tumor and CAFs
Supplementary Table 13: Uniquely Expressed Genes Tumor

Graphical Summary

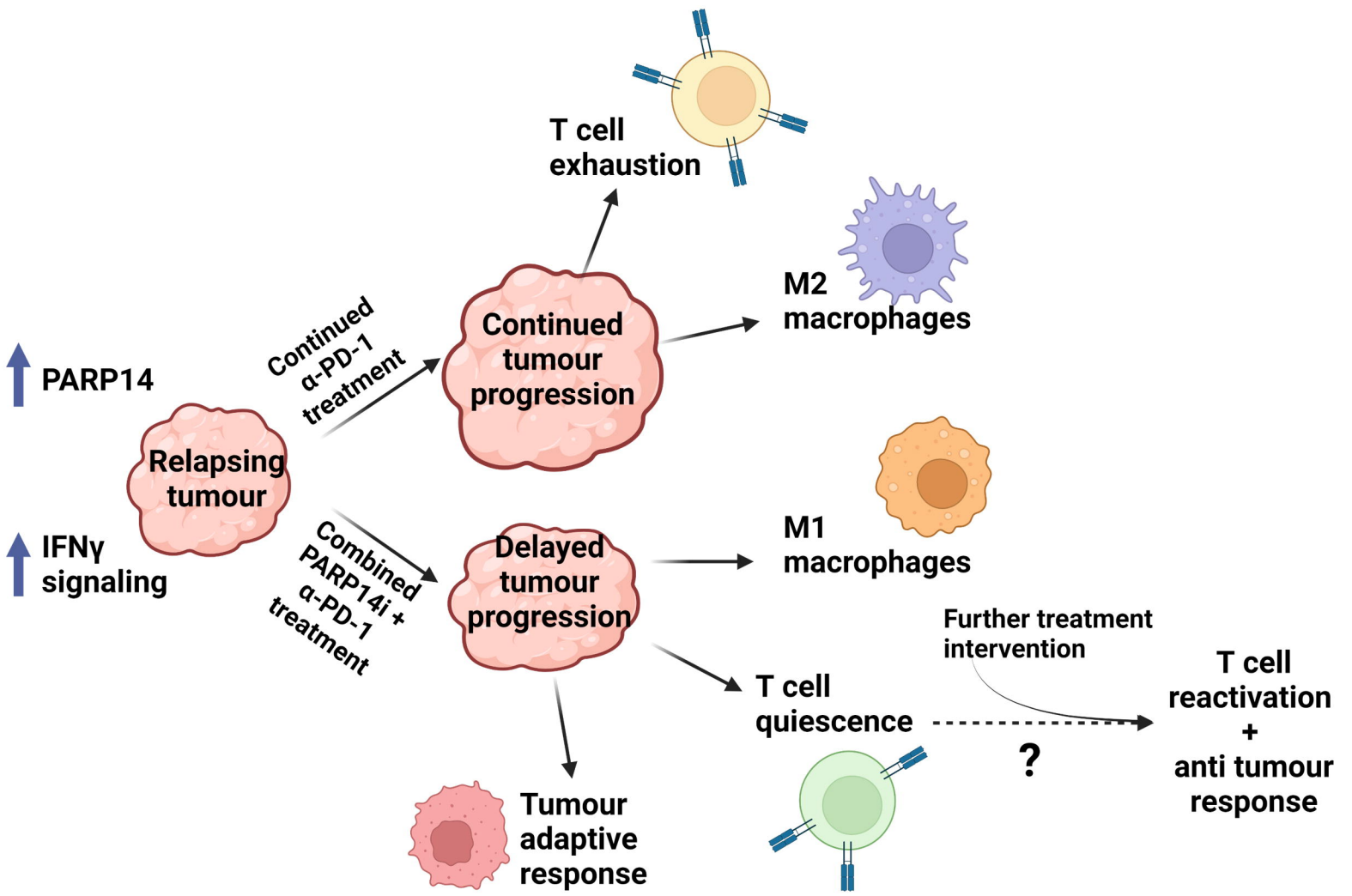

Fig 1

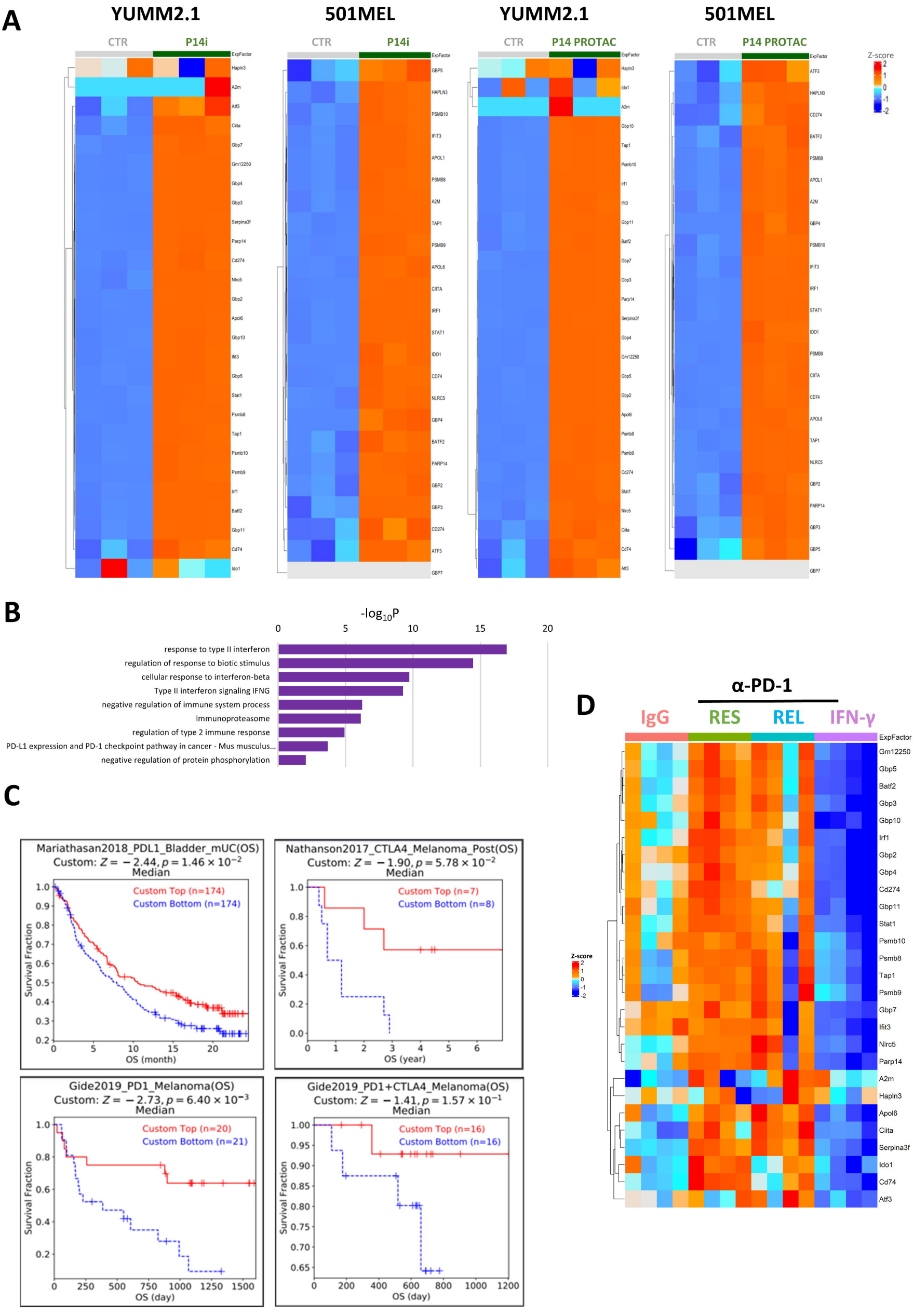
A
YUMM2.1
501MEL
YUMM2.1
501MEL
CTR
P14i
P14 PROTAC
ExpFactor
Z-score
B
-log10P
response to type II interfero
regulation of response to biotic stimulus
cellular response to interferon-beta
Type II interferon signaling IFNG
negative regulation of immune system process
Immunoproteasome
regulation of type 2 immune response
PD-L1 expression and PD-1 checkpoint pathway in cancer - Mus musculus...
negative regulation of protein phosphorylation
C
Mariathasan2018_PDL1_Bladder_mUC(OS)
Custom: Z = −2.44, p = 1.46 × 10−2
Median
Custom Top (n=174)
Custom Bottom (n=174)
Survival Fraction
OS (month)
Nathanson2017_CTLA4_Melanoma_Post(OS)
Custom: Z = −1.90, p = 5.78 × 10−2
Median
Custom Top (n=7)
Custom Bottom (n=8)
OS (year)
Gide2019_PD1_Melanoma(OS)
Custom: Z = −2.73, p = 6.40 × 10−3
Median
Custom Top (n=20)
Custom Bottom (n=21)
OS (day)
Gide2019_PD1+CTLA4_Melanoma(OS)
Custom: Z = −1.41, p = 1.57 × 10−1
Median
Custom Top (n=16)
Custom Bottom (n=16)
OS (day)
D
α-PD-1
IgG
RES
REL
IFN-γ
ExpFactor
Z-score

Fig 2

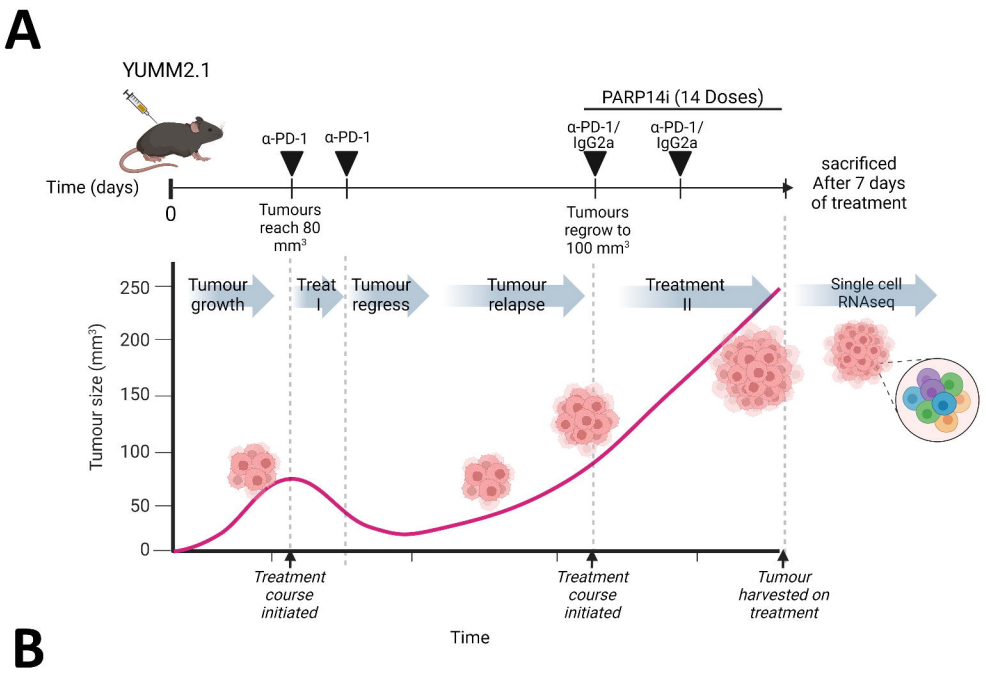
A
YUMM2.1
PARP14i (14 Doses)
α-PD-1
α-PD-1
α-PD-1/ IgG2a
α-PD-1/ IgG2a
Time (days)
0
Tumours reach 80 mm³
Tumours regrow to 100 mm³
sacrificed After 7 days of treatment
Tumour growth
Treat I
Tumour regress
Tumour relapse
Treatment II
Single cell RNAseq
Tumour size (mm³)
Treatment course initiated
Treatment course initiated
Tumour harvested on treatment
Time

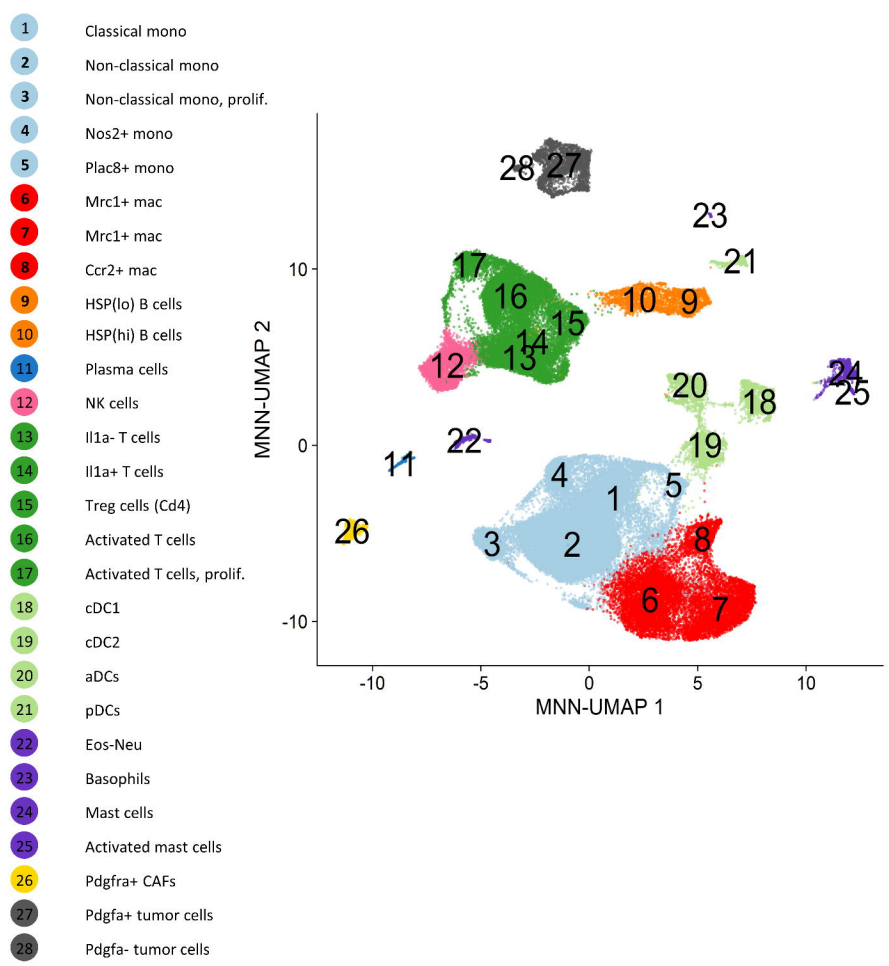
B
1 Classical mono
2 Non-classical mono
3 Non-classical mono, prolif.
4 Nos2+ mono
5 Plac8+ mono
6 Mrc1+ mac
7 Mrc1+ mac
8 Ccr2+ mac
9 HSP(lo) B cells
10 HSP(hi) B cells
11 Plasma cells
12 NK cells
13 Il1a- T cells
14 Il1a+ T cells
15 Treg cells (Cd4)
16 Activated T cells
17 Activated T cells, prolif.
18 cDC1
19 cDC2
20 aDCs
21 pDCs
22 Eos-Neu
23 Basophils
24 Mast cells
25 Activated mast cells
26 Pdgfra+ CAFs
27 Pdgfa+ tumor cells
28 Pdgfa- tumor cells
MNN-UMAP 2
MNN-UMAP 1

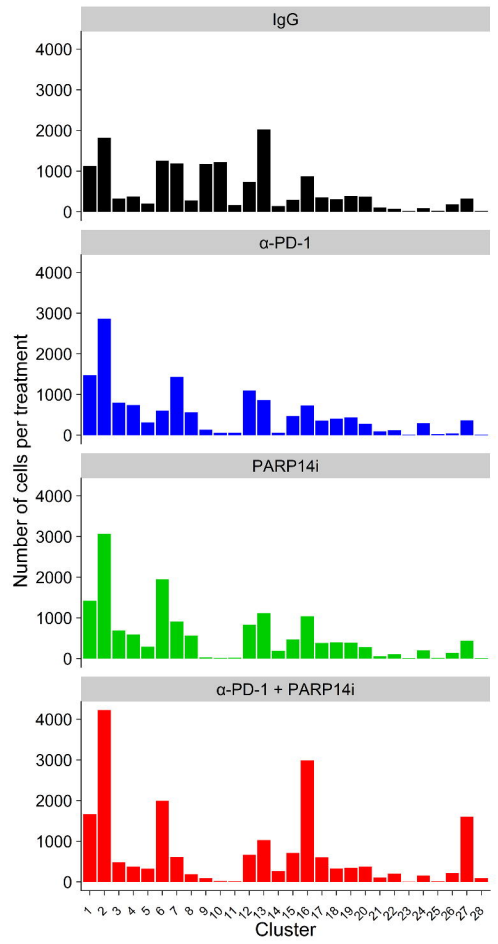
C
IgG
α-PD-1
PARP14i
α-PD-1 + PARP14i
Number of cells per treatment
Cluster

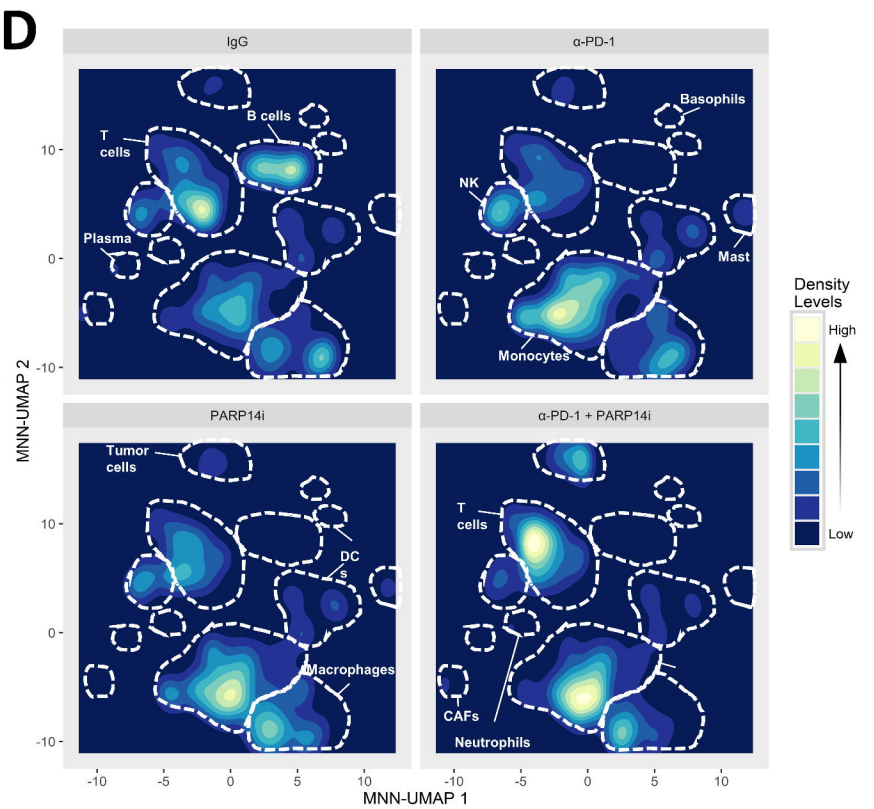
D
IgG
α-PD-1
PARP14i
α-PD-1 + PARP14i
T cells
B cells
Plasma
Basophils
NK
Mast
Monocytes
Tumor cells
DCs
Macrophages
T cells
CAFs
Neutrophils
Density Levels
High
Low
MNN-UMAP 2
MNN-UMAP 1

Fig 3

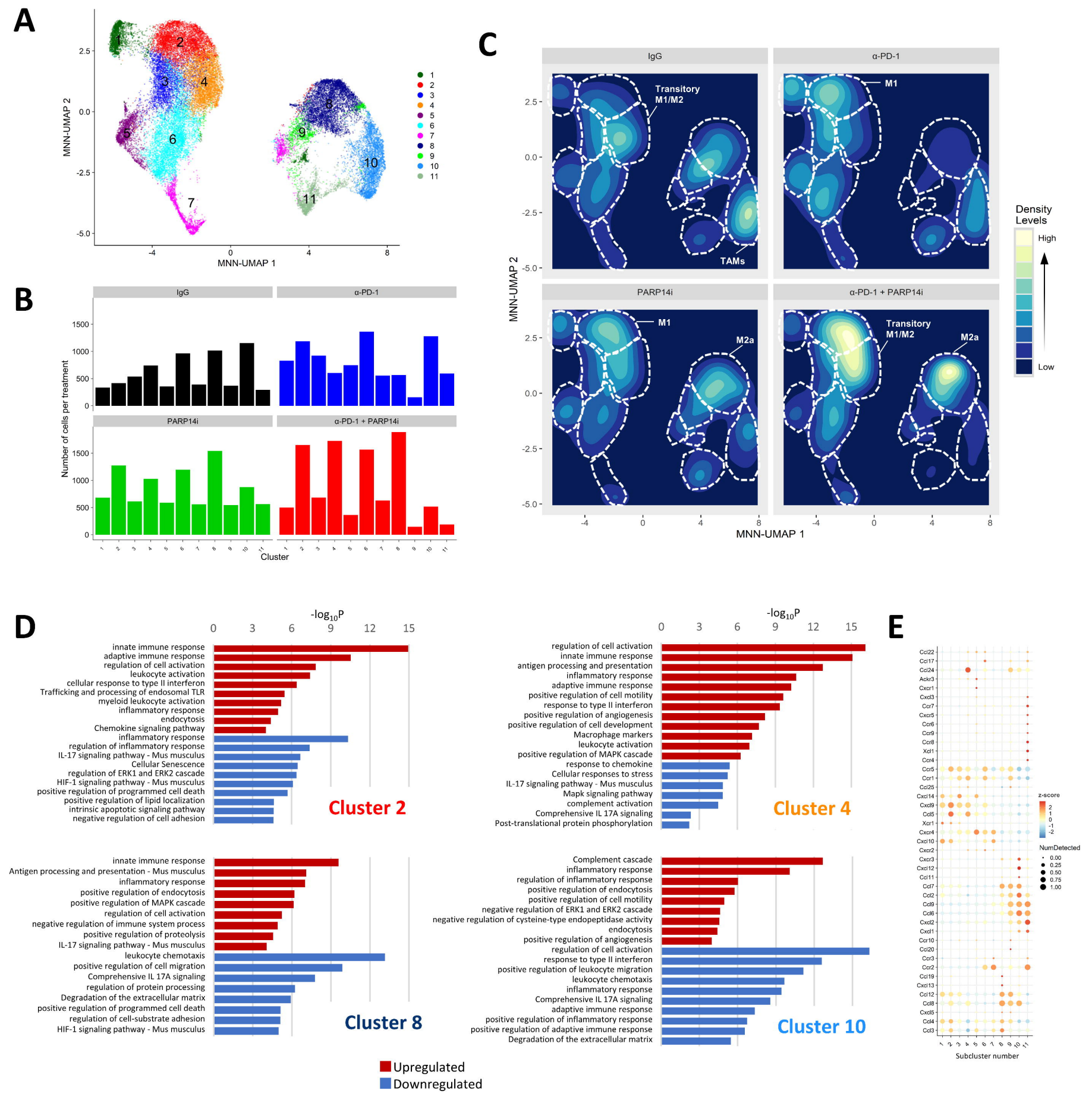
A
MNN-UMAP 1
MNN-UMAP 2
B
IgG
α-PD-1
PARP14i
α-PD-1 + PARP14i
Number of cells per treatment
Cluster
C
Transitory M1/M2
TAMs
M1
M2a
Density Levels
High
Low
D
-log10P
Cluster 2
innate immune response
adaptive immune response
regulation of cell activation
leukocyte activation
cellular response to type II interferon
Trafficking and processing of endosomal TLR
myeloid leukocyte activation
inflammatory response
endocytosis
Chemokine signaling pathway
inflammatory response
regulation of inflammatory response
IL-17 signaling pathway - Mus musculus
Cellular Senescence
regulation of ERK1 and ERK2 cascade
HIF-1 signaling pathway - Mus musculus
positive regulation of programmed cell death
positive regulation of lipid localization
intrinsic apoptotic signaling pathway
negative regulation of cell adhesion
Cluster 4
regulation of cell activation
innate immune response
antigen processing and presentation
inflammatory response
adaptive immune response
positive regulation of cell motility
response to type II interferon
positive regulation of angiogenesis
positive regulation of cell development
Macrophage markers
leukocyte activation
positive regulation of MAPK cascade
response to chemokine
Cellular responses to stress
IL-17 signaling pathway - Mus musculus
Mapk signaling pathway
complement activation
Comprehensive IL 17A signaling
Post-translational protein phosphorylation
Cluster 8
innate immune response
Antigen processing and presentation - Mus musculus
inflammatory response
positive regulation of endocytosis
positive regulation of MAPK cascade
regulation of cell activation
negative regulation of immune system process
positive regulation of proteolysis
IL-17 signaling pathway - Mus musculus
leukocyte chemotaxis
positive regulation of cell migration
Comprehensive IL 17A signaling
regulation of protein processing
Degradation of the extracellular matrix
positive regulation of programmed cell death
regulation of cell-substrate adhesion
HIF-1 signaling pathway - Mus musculus
Cluster 10
Complement cascade
inflammatory response
regulation of inflammatory response
positive regulation of endocytosis
positive regulation of cell motility
negative regulation of ERK1 and ERK2 cascade
negative regulation of cysteine-type endopeptidase activity
endocytosis
positive regulation of angiogenesis
regulation of cell activation
response to type II interferon
positive regulation of leukocyte migration
leukocyte chemotaxis
inflammatory response
Comprehensive IL 17A signaling
adaptive immune response
positive regulation of inflammatory response
positive regulation of adaptive immune response
Degradation of the extracellular matrix
Upregulated
Downregulated
E
z-score
NumDetected
Subcluster number
F
IgG
αPD1
PARP14i
α-PD-1 + PARP14i
Subcluster number
G
Rxra (11g)
Srebf1 (31g)
Irf4_extended (25g)
Runx3 (73g)
Cux1_extended (11g)
Nfia_extended (23g)
Nr1d1_extended (13g)
Klf2 (23g)
Klf3 (114g)
Etv1_extended (105g)
Dbp_extended (187g)
Rest (44g)
Tfdp1 (141g)
E2f8 (47g)
Nfyb (43g)
Regulon activity (%)
Subcluster number

Fig 4

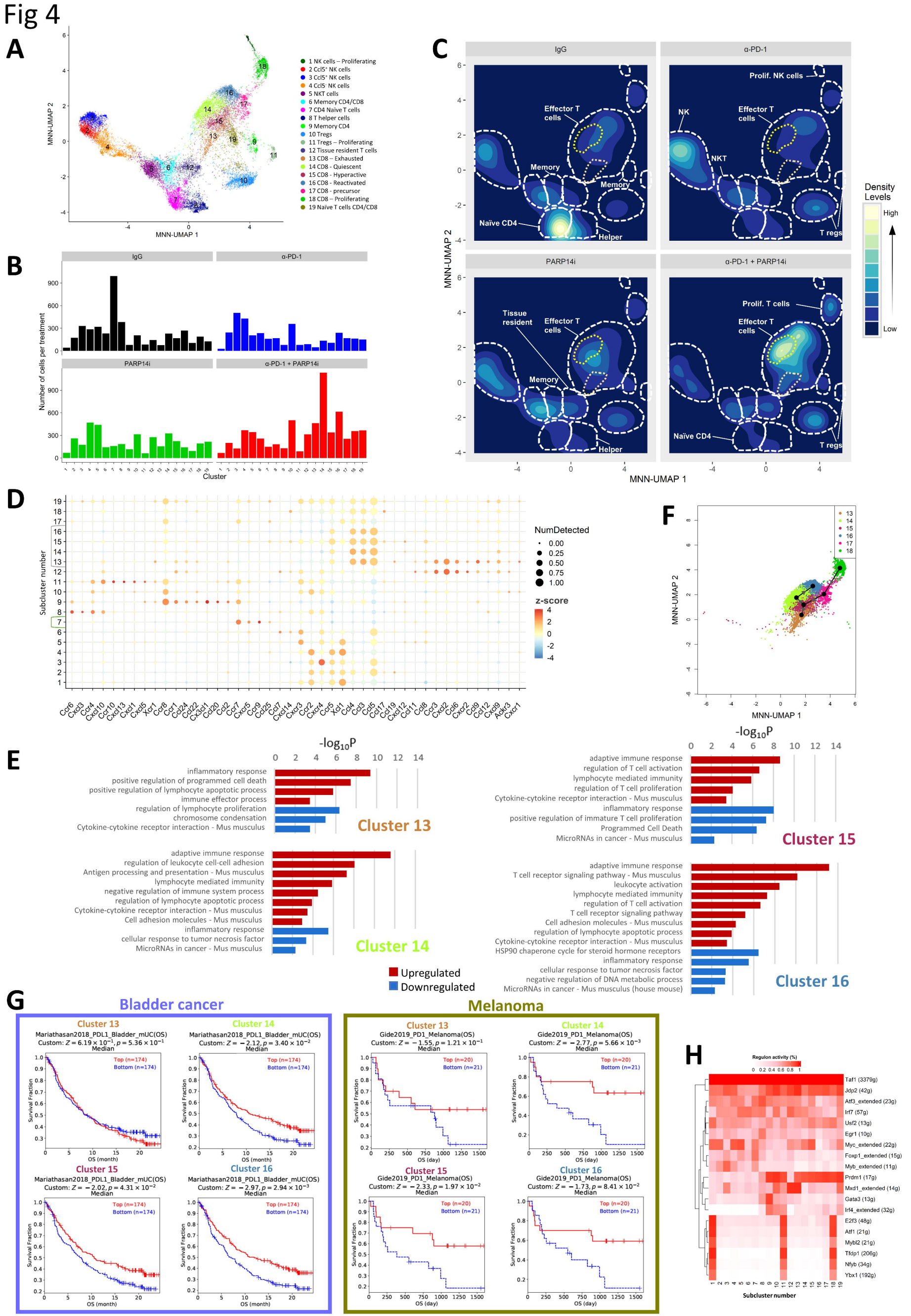
A
MNN-UMAP 1
MNN-UMAP 2
1 NK cells – Proliferating
2 Ccl5⁺ NK cells
3 Ccl5⁺ NK cells
4 Ccl5⁻ NK cells
5 NKT cells
6 Memory CD4/CD8
7 CD4 Naïve T cells
8 T helper cells
9 Memory CD4
10 Tregs
11 Tregs – Proliferating
12 Tissue resident T cells
13 CD8 – Exhausted
14 CD8 - Quiescent
15 CD8 - Hyperactive
16 CD8 - Reactivated
17 CD8 - precursor
18 CD8 – Proliferating
19 Naïve T cells CD4/CD8
B
IgG
α-PD-1
PARP14i
α-PD-1 + PARP14i
Number of cells per treatment
Cluster
C
IgG
α-PD-1
PARP14i
α-PD-1 + PARP14i
Effector T cells
Memory
Naïve CD4
Helper
Prolif. NK cells
NK
NKT
T regs
Tissue resident
Prolif. T cells
Density Levels
High
Low
MNN-UMAP 1
MNN-UMAP 2
D
Subcluster number
NumDetected
0.00
0.25
0.50
0.75
1.00
z-score
F
MNN-UMAP 1
MNN-UMAP 2
E
-log10P
inflammatory response
positive regulation of programmed cell death
positive regulation of lymphocyte apoptotic process
immune effector process
regulation of lymphocyte proliferation
chromosome condensation
Cytokine-cytokine receptor interaction - Mus musculus
Cluster 13
adaptive immune response
regulation of leukocyte cell-cell adhesion
Antigen processing and presentation - Mus musculus
lymphocyte mediated immunity
negative regulation of immune system process
regulation of lymphocyte apoptotic process
Cytokine-cytokine receptor interaction - Mus musculus
Cell adhesion molecules - Mus musculus
inflammatory response
cellular response to tumor necrosis factor
MicroRNAs in cancer - Mus musculus
Cluster 14
Upregulated
Downregulated
adaptive immune response
regulation of T cell activation
lymphocyte mediated immunity
regulation of T cell proliferation
Cytokine-cytokine receptor interaction - Mus musculus
inflammatory response
positive regulation of immature T cell proliferation
Programmed Cell Death
MicroRNAs in cancer - Mus musculus
Cluster 15
adaptive immune response
T cell receptor signaling pathway - Mus musculus
leukocyte activation
lymphocyte mediated immunity
regulation of T cell activation
T cell receptor signaling pathway
Cell adhesion molecules - Mus musculus
regulation of lymphocyte apoptotic process
Cytokine-cytokine receptor interaction - Mus musculus
HSP90 chaperone cycle for steroid hormone receptors
inflammatory response
cellular response to tumor necrosis factor
negative regulation of DNA metabolic process
MicroRNAs in cancer - Mus musculus (house mouse)
Cluster 16
G
Bladder cancer
Melanoma
Cluster 13
Mariathasan2018_PDL1_Bladder_mUC(OS)
Custom: Z = 6.19 × 10⁻¹, p = 5.36 × 10⁻¹
Cluster 14
Mariathasan2018_PDL1_Bladder_mUC(OS)
Custom: Z = −2.12, p = 3.40 × 10⁻²
Cluster 15
Mariathasan2018_PDL1_Bladder_mUC(OS)
Custom: Z = −2.02, p = 4.31 × 10⁻²
Cluster 16
Mariathasan2018_PDL1_Bladder_mUC(OS)
Custom: Z = −2.97, p = 2.94 × 10⁻³
Cluster 13
Gide2019_PD1_Melanoma(OS)
Custom: Z = −1.55, p = 1.21 × 10⁻¹
Cluster 14
Gide2019_PD1_Melanoma(OS)
Custom: Z = −2.77, p = 5.66 × 10⁻³
Cluster 15
Gide2019_PD1_Melanoma(OS)
Custom: Z = −2.33, p = 1.97 × 10⁻²
Cluster 16
Gide2019_PD1_Melanoma(OS)
Custom: Z = −1.73, p = 8.41 × 10⁻²
Median
Top (n=174)
Bottom (n=174)
Top (n=20)
Bottom (n=21)
Survival Fraction
OS (month)
OS (day)
H
Regulon activity (%)
Taf1 (3379g)
Jdp2 (42g)
Atf3_extended (23g)
Irf7 (57g)
Usf2 (13g)
Egr1 (10g)
Myc_extended (22g)
Foxp1_extended (15g)
Myb_extended (11g)
Prdm1 (17g)
Mxd1_extended (14g)
Gata3 (13g)
Irf4_extended (32g)
E2f3 (48g)
Atf1 (21g)
Mybl2 (21g)
Tfdp1 (206g)
Nfyb (34g)
Ybx1 (192g)
Subcluster number

Fig 5

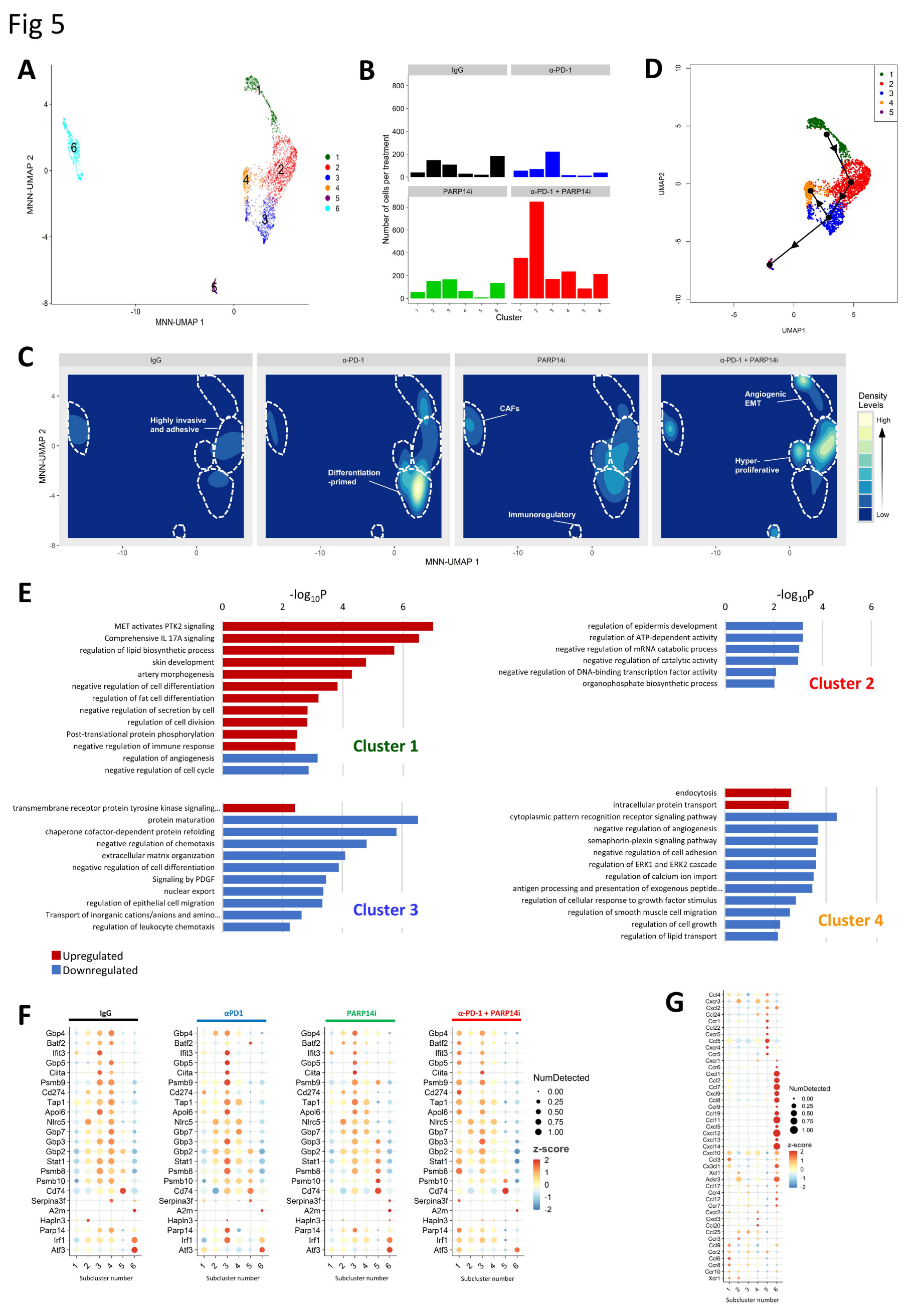
A
MNN-UMAP 2
MNN-UMAP 1
1
2
3
4
5
6
B
IgG
α-PD-1
PARP14i
α-PD-1 + PARP14i
Number of cells per treatment
Cluster
D
UMAP2
UMAP1
C
Highly invasive and adhesive
Differentiation -primed
CAFs
Immunoregulatory
Angiogenic EMT
Hyper-proliferative
Density Levels
High
Low
E
-log10P
MET activates PTK2 signaling
Comprehensive IL 17A signaling
regulation of lipid biosynthetic process
skin development
artery morphogenesis
negative regulation of cell differentiation
regulation of fat cell differentiation
negative regulation of secretion by cell
regulation of cell division
Post-translational protein phosphorylation
negative regulation of immune response
regulation of angiogenesis
negative regulation of cell cycle
Cluster 1
regulation of epidermis development
regulation of ATP-dependent activity
negative regulation of mRNA catabolic process
negative regulation of catalytic activity
negative regulation of DNA-binding transcription factor activity
organophosphate biosynthetic process
Cluster 2
transmembrane receptor protein tyrosine kinase signaling...
protein maturation
chaperone cofactor-dependent protein refolding
negative regulation of chemotaxis
extracellular matrix organization
negative regulation of cell differentiation
Signaling by PDGF
nuclear export
regulation of epithelial cell migration
Transport of inorganic cations/anions and amino...
regulation of leukocyte chemotaxis
Cluster 3
endocytosis
intracellular protein transport
cytoplasmic pattern recognition receptor signaling pathway
negative regulation of angiogenesis
semaphorin-plexin signaling pathway
negative regulation of cell adhesion
regulation of ERK1 and ERK2 cascade
regulation of calcium ion import
antigen processing and presentation of exogenous peptide...
regulation of cellular response to growth factor stimulus
regulation of smooth muscle cell migration
regulation of cell growth
regulation of lipid transport
Cluster 4
Upregulated
Downregulated
F
IgG
αPD1
PARP14i
α-PD-1 + PARP14i
Gbp4
Batf2
Ifit3
Gbp5
Ciita
Psmb9
Cd274
Tap1
Apol6
Nlrc5
Gbp7
Gbp3
Gbp2
Stat1
Psmb8
Psmb10
Cd74
Serpina3f
A2m
Hapln3
Parp14
Irf1
Atf3
Subcluster number
NumDetected
z-score
G
Ccl4
Cxcr3
Cxcl2
Ccl24
Ccr1
Ccl22
Cxcr5
Ccl5
Cxcr4
Ccr5
Cxcr1
Ccr6
Cxcl1
Ccl2
Ccl7
Cxcl9
Ccl8
Ccr9
Ccl19
Ccl11
Cxcl5
Cxcl12
Cxcl13
Cxcl14
Cxcl10
Ccl3
Cx3cl1
Xcl1
Ackr3
Ccl17
Ccr4
Ccl12
Ccr7
Cxcr2
Cxcl3
Ccl20
Ccl25
Ccr3
Ccl9
Ccr2
Ccl6
Ccr8
Ccr10
Xcr1
Subcluster number
NumDetected
z-score